

Polarized epidermal growth factor secretion ensures robust vulval cell fate specification in *Caenorhabditis* *elegans*

Louisa Mereu^{1,2,*}, Matthias K. Morf^{1,2,3,*}, Silvan Spiri^{1,2,*}, Peter Gutierrez⁴, Juan M. Escobar-Restrepo^{1,5}, Michael Daube¹, Michael Walser¹ and Alex Hajnal^{1,°}

* These authors contributed equally to this work.

¹Institute of Molecular Life Sciences, University of Zürich, Winterthurerstrasse 190, CH-8057 Zürich, Switzerland

²Molecular Life Science PhD Program, University and ETH Zürich, CH-8057 Zürich, Switzerland

³ present address: Swiss Laboratory for Doping Analyses, University Center of Legal Medicine, Lausanne and Geneva, Centre Hospitalier Universitaire Vaudois and University of Lausanne, Lausanne, Switzerland

⁴ present address: Kantonsschule Olten, Fachschaften Biologie und Chemie, Hardfeldstrasse 53, 4600 Olten, Switzerland

⁵ present address: Roche Diagnostics, Industriestrasse 7 CH-6343, Rotkreuz, Switzerland

[°]Corresponding author: alex.hajnal@mls.uzh.ch

Key words: *C. elegans*, epidermal growth factor, polarity, cell fate.

Abstract

The anchor cell (AC) in *C. elegans* secretes an EGF homolog that induces adjacent vulval precursor cells (VPCs) to differentiate. The EGF receptor in the nearest VPC sequesters the limiting EGF amounts released by the AC to prevent EGF from spreading to distal VPCs. Here, we show that not only EGFR localization in the VPCs but also EGF polarity in the AC is necessary for robust fate specification. The AC secretes EGF in a directional manner towards the nearest VPC. Loss of AC polarity causes signal spreading and, when combined with MAPK pathway hyperactivation, the ectopic induction of distal VPCs. In a screen for genes preventing distal VPC induction, we identified *sra-9* and *nlp-26* as genes specifically required for polarized EGF secretion. *sra-9(lf)* and *nlp-26(lf)* mutants exhibit errors in vulval fate specification, reduced precision in VPC to AC alignment and increased variability in MAPK activation. *sra-9* encodes a seven-pass trans-membrane receptor acting in the AC and *nlp-26* a neuropeptide-like protein expressed in the VPCs. SRA-9 and NLP-26 may transduce a feedback signal to channel EGF secretion towards the nearest VPC.

Introduction

Intercellular communication relies on the spatially and temporally controlled release of signaling molecules by the signal emitting cells. Members of the Epidermal Growth Factor (EGF) family are involved in a variety of cell fate decisions in all metazoans (Massagué and Pandiella, 1993). Secreted EGF ligands bind to receptor tyrosine kinases of the ErbB/EGFR family, which activate different intracellular signaling pathways, such as the RAS/MAPK, the PI3K/AKT, JAK/STAT or the PLC pathways, depending on the cellular context (Hynes and MacDonald, 2009). While many studies have focused on the mechanisms controlling the polarized secretion, internalization and recycling of the EGF receptors (Sorkin and Goh, 2008), less is known about the factors controlling the intracellular trafficking of the EGF family ligands. EGF ligands are typically produced as transmembrane precursor proteins. They can either act as a membrane-bound form in a juxtacrine manner, or be cleaved by intracellular rhomboid family proteases (Urban et al., 2001) and extracellular metalloproteases, allowing them to be released and signal at a distance (Massagué and Pandiella, 1993). The concentration and temporal duration of an EGF signal can lead to differential responses in the signal receiving cells, for example during cell fate specification (Katz et al., 1995), apoptosis (Iwamoto et al., 1999) or cell migration (Wyckoff et al., 2004). Moreover, by controlling the subcellular localization of EGF ligands, cells can regulate ligand availability and add directionality to the signal (Dempsey et al., 1997). The basolateral versus apical sorting of transforming growth factor alpha in cultured epithelial cells is important to restrict EGFR activation to the basolateral compartment (Singh and Coffey, 2014). One of the few examples demonstrating polarized EGF secretion during animal development in vivo is the release of the *Drosophila* EGF ligand Spitz by photoreceptor neurons (Yogev et al., 2010).

The *Caenorhabditis elegans* genome each encodes a single EGF-like growth factor, termed *lin-3*, and an EGFR receptor homolog, termed *let-23* (Sundaram, 2013). Thus, the lack of genetic

redundancy has greatly simplified the analysis of the EGF signaling network in *C. elegans*. The LIN-3/LET-23 pathway controls many cell fate decisions during larval development as well as various adult functions. In particular, the development of the *C. elegans* hermaphrodite vulva is an excellent model to study cell fate decisions controlled by EGF signaling at single cell resolution (Sternberg, 2005). During the first larval stage (L1), 12 epidermal Pn.p cells (P1.p to P12.p) are generated in the ventral epidermis (**Fig. 1**). Six Pn.p cells in the mid-body region (P3.p to P8.p) are specified by a Wingless signal to become vulval precursor cells (VPCs) that express LET-23 and are competent to differentiate into vulval cells (Eisenmann et al., 1998). VPC differentiation is induced by the uterine anchor cell (AC) located dorsally to the VPCs in the somatic gonad (Kimble, 1981). From the L2 stage on, the AC expresses LIN-3 (Hill and Sternberg, 1992). Even though LIN-3 is secreted to the plasma membrane as a type I trans-membrane protein similar to transforming growth factor alpha, the AC can induce distant VPCs without making direct contact (Hill and Sternberg, 1992). Thus, at least a fraction of LIN-3 must be released from the AC, which probably occurs by shedding of the extracellular domain rather than by intracellular proteolysis, as the intracellular rhomboid protease ROM-1 does not act in the AC (Dutt et al., 2004). The LIN-3 signal activates via its receptor LET-23 the RAS/MAPK pathway the primary (1°) cell fate in the nearest VPC P6.p (**Fig. 1**) (Sternberg, 2005; Sundaram, 2013). Strong RAS/MAPK signaling in P6.p leads to the up-regulation of LET-23 and of DSL family NOTCH ligands (Chen and Greenwald, 2004; Greenwald and Kovall, 2013). The latter activate the LIN-12 NOTCH receptor in the adjacent VPCs, P5.p and P7.p by lateral signaling to repress the 1° and induce the secondary (2°) cell fate (Berset et al., 2001; Yoo et al., 2004). The distal VPCs (P3.p, P4.p and P8.p) that receive neither the inductive LIN-3 nor the lateral DSL signal adopt the un-induced, tertiary (3°) cell fate. The 3° VPCs divide once and then fuse with the surrounding epidermis (hyp7). This interplay between the

EGFR/RAS/MAPK and NOTCH pathways results in an invariant 2°-1°-2° vulval cell fate pattern.

Vulval induction in the wild-type is extremely robust (Félix and Barkoulas, 2012). P6.p, the VPC located closest to the AC adopts the 1° cell fate when animals are raised under standard conditions. Rare errors in vulval fate specification, such as shifts in the 1° fate from P6.p to another VPC or the hyperinduction of extra VPCs, only occur when animals are grown under suboptimal conditions, for example at low temperature or under food starvation (Braendle and Félix, 2008). The AC produces a limiting amount of the inductive LIN-3 signal, while LET-23 expressed by the VPCs provides excess LIN-3 binding sites (Barkoulas et al., 2013; Simske and Kim, 1995). Hence, the nearest VPC P6.p sequesters most of the inductive signal and thereby prevents the induction of additional, more distal VPCs (Hajnal et al., 1997). Efficient LIN-3 sequestering and vulval induction require the localization of LET-23 to the basolateral membrane compartment of the VPCs facing the AC (Whitfield et al., 1999). Basolateral LET-23 localization is maintained by the tripartite LIN-2/LIN-7/LIN-10 receptor localization complex (Kaeck et al., 1998). The apical mislocalization of LET-23, for example in *lin-2(0)* mutants, leads to a strong reduction in vulval induction and a penetrant vulvaless (Vul) phenotype (Hoskins et al., 1996). However, in combination with a loss-of-function (*lf*) mutation in the RAS GTPase-activating protein GAP-1, which causes a mild hyperactivation of the RAS/MAPK pathway, apical LET-23 mislocalization causes the ectopic induction of VPCs distant from the AC and a multivulva (Muv) phenotype (Hajnal et al., 1997). This finding has been attributed to an expanded range of the LIN-3 signal caused by the loss of LIN-3 sequestering by P6.p.

Here, we show that not only basolateral LET-23 localization in the VPCs, but also the polarized secretion of LIN-3 by the AC towards the 1° VPC is necessary for robust vulval induction. Furthermore, an unbiased screen for genes controlling polarized LIN-3 secretion has identified

a putative neuropeptide-like ligand and a G-protein coupled receptor required for LIN-3 polarity and robust vulval induction .

Results

Depolarization of the AC causes ectopic and shifted vulval induction

In wild-type *C. elegans* larvae, the three proximal VPCs P5.p, P6.p and P7.p are induced to adopt vulval cell fates. Thus, the vulval induction index (VI) in the wild-type is exactly 3. A *lf* mutation in the RAS-GAP gene *gap-1(ga133lf)* enhances the activity of the inductive RAS/MAPK signaling pathway, but not enough to cause the induction of additional VPCs (Hajnal et al., 1997). Only one in 300 *gap-1(lf)* animals exhibited a hyper-induced phenotype (**Fig. 2A,E,F**). *gap-1(lf)* can thus be utilized as a sensitized genetic background to detect changes in LIN-3 distribution, such as the reduced LIN-3 sequestering caused by apical LET-23 mislocalization (Hajnal et al., 1997).

The *unc-6* gene encodes a Netrin homologue that is secreted by ventral cord motorneurons and polarizes the AC along the dorso-ventral axis towards the VPCs that are aligned on the ventral midline (Ziel et al., 2009). Surprisingly, *unc-6(ev400lf); gap-1(ga133lf)* double mutants exhibited a 20% penetrant hyper-induced phenotype due to the ectopic induction of distal VPCs (**Fig. 2C,F**). Similar hyper-induced phenotypes were observed after combining *gap-1(lf)* with mutations in other known AC polarity regulators, such as the Netrin receptor *unc-40* (Ziel et al., 2009) or the *unc-40* downstream effector *madd-2* (**Fig. 2D,F**) (Morf et al., 2013). Furthermore, depolarization of the AC by *unc-6(lf)* enhanced the Vul phenotype and reduced the VI of the *lin-3(e1417)* reduction-of-function-allele or the *let-23(sy1)* receptor mislocalization mutant (**Fig. 2E,G**).

To test if the hyper-induced vulval phenotype is caused by a depolarization of the AC, we introduced an *unc-40::gfp* rescue minigene (*zhEx668*) driven by the AC-specific *mk62-63 cdh-3* promoter fragment (Ziel et al., 2009) into the *unc-40(lf); gap-1(lf)* background. The *unc-*

40::gfp transgene was expressed in the AC and in ventral nerve cord (VNC) neurons of L2 of mid-L2 to early L3 larvae, but not in the VPCs (**Fig. S1A,B**). Three independent transgenic lines exhibited a partial suppression of the hyper-induced phenotype and a reduced VI of *unc-40(lf); gap-1(lf)* double mutants (**Fig. S1C**). Since the VNCs neurons are unlikely to affect VPC differentiation, *unc-40* probably acts in the AC to inhibit vulval induction.

In wild-type larvae, the AC invariably induces the most proximal VPC P6.p to adopt the 1° cell fate (Braendle and Félix, 2008). Besides the changes in vulval induction, we also observed shifts of the 1° fate from P6.p to P5.p, or rarely to P7.p, in *unc-6(lf)* single as well as in *unc-6(lf); gap-1(lf)* double mutants (**Fig. 2E,H**).

These findings suggested that dorso-ventral AC polarity is needed for the robust induction of the 1° fate in P6.p. Similar to the case of apical LET-23 mislocalization, loss of AC polarity may affect the range and distribution of the inductive LIN-3 signal among the VPCs.

Polarized distribution of LIN-3 in the AC

One possible explanation for the vulval phenotypes observed in AC polarity mutants is that the AC normally secretes LIN-3 in a polarized fashion in the direction of the closest VPC. To directly observe LIN-3 localization in the AC, we inserted an mNeongreen (mNGr) fluorophore cassette into the *lin-3* locus directly after the predicted signal sequence (after Leu24 in LIN-3A) and N-terminally to the EGF domain using CRISPR/Cas9-mediated genome engineering (*mNGr::lin-3(zh112)*, **Fig. S2**) (Dickinson et al., 2015). *mNGr::lin-3(zh112)* animals exhibited an overall wild-type phenotype without any obvious defects in vulval development, indicating that the mNGr::LIN-3 fusion protein retains its activity at levels comparable to the wild-type LIN-3 protein. In L2 and L3 larvae, mNGr::LIN-3 expression was detected in intracellular punctae and on the basal cortex of the AC (**Fig. 3A,C,E**). No extracellular mNGr::LIN-3 signal could be detected, suggesting that after its secretion to the plasma membrane the majority of

mNGr::LIN-3 remains attached to the AC surface, or that a cleavage product of the mNGr::LIN-3 protein is released from the AC and rapidly taken up by the adjacent VPCs or degraded. The same localization pattern was observed with a multi-copy GFP::LIN-3 transgene (*zhIs67*), in which the GFP tag had been inserted at the same position as in the endogenous *mNGr::lin-3(zh112)* reporter strain (**Fig. S3**).

In wild-type larvae, mNGr::LIN-3 was enriched towards the ventral cortex of the AC from the mid-L2 stage on until the mid-L3 stage (**Fig. 3A,C,E**). To quantify LIN-3 polarity, we recorded optical sections through the AC of animals expressing mNGr::LIN-3 together with the *mCherry::PLC δ^{PH}* reporter that labels phosphatidylinositol-(4,5)-bisphosphate (PIP₂)-rich membranes and serves as a global AC polarity marker (Ziel et al., 2009). After measuring the average intensities in summed z-projections in the ventral and dorsal half of the AC, we calculated for each animal a dorso-ventral polarity index (I_{DV}) for both mNGr::LIN-3 and PIP₂ by dividing the signal intensity in the ventral by the intensity in the dorsal half of the AC (see materials and methods). We first measured the mNGr::LIN-3 and PIP₂ I_{DV} in wild-type larvae between the early L2 and mid L3 stages before the first round of VPC divisions. The developmental stage was assigned according to the animal's gonad length as described in materials and methods (Kimble and Hirsh, 1979). The average mNGr::LIN-3 I_{DV} was around 1.3 at all three stages, with only a few cases showing an I_{DV} below 1 (**Fig. 3H,J,L**). Around 90% of the animals across the three stages analyzed had an I_{DV} higher than 1.1 (**Fig. 3H,J,L**). The PIP₂ global polarity marker showed a slightly stronger polarization of the AC with an average I_{DV} above 1.5 and an $I_{DV} \geq 1.2$ in around 90% of the animals at the three stages analyzed (**Fig. 3G,I,K**).

Taken together, the endogenous *mNGr::lin-3* and transgenic *gfp::lin-3* reporters revealed a polarized distribution of LIN-3 in the AC before and during vulval induction, but no extracellular signal was detectable.

LIN-3 polarity is reduced in *unc-6* netrin mutants

We next tested if a global depolarization of the AC affects LIN-3 polarity. The *unc-6(ev400)* loss-of-function allele causes a strong reduction in AC polarity that manifests in a more uniform PIP₂ localization. Accordingly, the average PIP₂ I_{DV} was decreased in *unc-6(lf)* mutants from the mid L2 stage on, such that fewer than 50% of the mid to late L2 larvae had a PIP₂ I_{DV} greater than 1.2 (**Fig. 3B,D,G,I**). PIP₂ polarity remained reduced in early to mid L3 *unc-6(lf)* larvae, though the effect was less pronounced (**Fig. 3F,K**).

LIN-3 polarity was also decreased in *unc-6(lf)* mutants (**Fig. 3B,D,F**). Especially, in mid to late L2 larvae, the time period when the AC signal selects the 1° VPC, the LIN-3 I_{DV} was below 1.1 in around half of the *unc-6(lf)* mutants analyzed (**Fig. 3H,J**). By the mid L3 stage, the effect of *unc-6(lf)* on LIN-3 polarity was less pronounced (**Fig. 3L**). Moreover, we observed a strong correlation between LIN-3 and PIP₂ polarity when testing on a per animal basis. There was a significant increase in the fraction of animals showing both PIP₂ and LIN-3 depolarization in *unc-6(lf)* animals compared to the wild-type (**Fig. S4**).

We conclude that the polarized distribution of LIN-3 in the AC depends on the global polarity established by the UNC-6 Netrin signal.

A whole-genome RNAi screen for ectopic vulval induction identifies genes specifically controlling LIN-3 polarity

The observation that a depolarization of the AC in the sensitized *gap-1(lf)* background causes ectopic vulval induction and a Muv phenotype opened the possibility to conduct a systematic screen for global AC polarity regulators and possibly also for specific regulators of LIN-3 polarity. To this aim, we performed a genome-wide RNAi screen in an *rrf-3(pk1426); gap-1(gal133)* hypersensitive background and searched for animals exhibiting a Muv phenotype

(Simmer et al., 2002). Through this approach, we identified 51 primary candidate genes that showed a reproducible Muv phenotype upon RNAi knock-down in the *rrf-3(pk1426); gap-1(gal33)* background (**Table S1**). Among the candidates identified were three genes previously known to act in the UNC-6 Netrin pathway that polarizes the AC; *unc-40*, *unc-73* and *madd-2* (highlighted in green in **Table S1**,) (Alexander et al., 2010; Morf et al., 2013; Ziel et al., 2009). In order to search for genes specifically regulating polarized LIN-3 localization in the AC, we performed a rescreen in a strain carrying the PIP₂ global AC polarity marker together with the multi-copy GFP::LIN-3 transgene *zhIs67* to increase signal intensity. This approach allowed us to identify candidates specifically changing LIN-3 distribution without affecting global AC polarity. Three of the 51 primary candidates exhibited altered GFP::LIN-3 but unchanged PIP₂ localization after RNAi knock-down. Those genes were *srh-247*, *nlp-26* and *sra-9* (**Table S1**, highlighted in orange). *sra-9* and *srh-247* encode putative seven-pass transmembrane G-protein coupled receptors (GPCRs) (Troemel et al., 1995), and *nlp-26* a secreted neuropeptide-like protein (Nathoo et al., 2001). For none of these genes has a role during vulval development been reported so far. Since RNAi of *srh-247* showed a weaker and more variable phenotype, we focused our further analysis on the *sra-9* and *nlp-26* genes.

LIN-3 polarity is reduced in *sra-9* and *nlp-26* mutants, while general AC polarity is not altered

To confirm the RNAi phenotypes, we generated *sra-9(lf)* and *nlp-26(lf)* mutations using the CRISPR/Cas9 system (Arribere et al., 2014; Dickinson et al., 2015). The *sra-9(zh108)* allele contains a 2.5 kb deletion spanning the entire coding region, while the *gfp::nlp-26(zh113)* allele carries a *gfp* insertion in the predicted signal peptide, generating a premature stop codon before the neuropeptide sequence. The endogenous *gfp::nlp-26(zh113)* reporter did not show any GFP expression, indicating that NLP-26 is expressed at very low levels.

We detected no significant differences in PIP₂ polarity in *sra-9(lf)* or *nlp-26(lf)* mutants at the different stages analyzed (**Fig. 4A-F,H,J**). Thus, *sra-9* and *nlp-26* are not required for global AC polarity. However, LIN-3 polarity in *sra-9(lf)* and *nlp-26(lf)* mutants was significantly reduced at the mid and late L2 stages, and to a lesser extent also in early to mid L3 larvae (**Fig. 4A-F,G,I**). In particular, the fraction of animals showing a LIN-3 I_{DV} >1.1 was reduced in *sra-9(lf)* and *nlp-26(lf)* mutants (**Fig. 4G,I**). After the mid L3 stage, when the VPC fates had been determined and the first round of VPC division had been completed, there was no significant difference in LIN-3 polarity between *sra-9(lf)* and *nlp-26(lf)* mutants and the wild-type (data not shown). In contrast to *unc-6(lf)* mutants, LIN-3 and PIP₂ polarity did not correlate in *sra-9(lf)* and *nlp-26(lf)* mutants when analyzed at the level of individual animals. There was a significant increase in the fraction of animals with depolarized LIN-3 that maintained polarized PIP₂ expression (**Fig. S4**). Thus, SRA-9 and NLP-26 are required for LIN-3 polarity independently of global AC polarity. Moreover, *sra-9(lf)* and *nlp-26(lf)* mutants did not show defects in AC invasion or vulval morphogenesis, two processes that depend on global AC polarity and are perturbed in *unc-6(lf)* mutants (Estes and Hanna-Rose, 2009; Ziel et al., 2009). These results indicate that the asymmetric distribution of LIN-3 in the overall polarized AC is not the default state, but rather an actively regulated process.

***sra-9* and *nlp-26* mutants exhibit an increased error rate in vulval induction and more variable MPK-1 ERK activity**

sra-9(lf) and *nlp-26(lf)* mutants exhibited hyper- or hypo-induced vulval phenotypes at a low frequency when combined with the *gap-1(lf)* mutation (**Fig. 5A**). Rarely, even *nlp-26(lf)* single mutants exhibited abnormal vulval induction. In addition, we observed 1° cell fate shifts from P6.p to P5.p in *nlp-26(lf)* single as well as in *sra-9(lf); gap-1(lf)* double mutants (**Fig. 5B**). Given the increased error rate in vulval induction in *sra-9(lf)* and *nlp-26(lf)* mutants, we

examined whether the loss of LIN-3 polarity affects MAP kinase MPK-1 activation in the VPCs, using an ERK-nKTR biosensor (de la Cova et al., 2017). Briefly, upon phosphorylation by MPK-1 the ERK-nKTR::mClover protein translocates from the nucleus to the cytoplasm of the VPCs. By co-expressing a nuclear mCherry::H2B marker together with the ERK-nKTR::mClover biosensor on a single bi-cistronic mRNA, MPK-1 activity can be quantified as the ratio of the nuclear mCherry::H2B (red) signal intensity divided by the nuclear ERK-nKTR::mClover (green) signal intensity (**Fig. 5C-E**). For each VPC and animal, the red/green ratio was normalized to the mean of the ratios in P4.p through P8.p in the respective animal (**Fig. 5F-I**). (P3.p was not analyzed since it only assumes a VPC fate in around 50% of the animals.). In wild-type larvae, MPK-1 activity was highest in P6.p in 91% of the animals, consistent with published data of de la Cova et al. (2017) (**Fig. 5F,K**). In *unc-6(lf)* mutants, the difference between MPK-1 activity in P6.p and the other VPCs was overall diminished, and the frequency of animals exhibiting highest MPK-1 activity in P6.p was reduced to 71% (**Fig. 5G,K**). Also in *sra-9(lf)* and *nlp-26(lf)* mutants, we measured a greater variability in MPK-1 activity with a significant fraction of animals showing average or below average MPK-1 activity in P6.p (**Fig. 5H-K**).

Thus, the robust MPK-1 activation observed in P6.p of wild-type larvae is perturbed by global AC depolarization in *unc-6(lf)* mutants or by specific loss of LIN-3 polarity in *sra-9(lf)* or *nlp-26(lf)* mutants. This increased variability in MPK-1 activity after the loss of LIN-3 polarity in the AC may underlie the elevated error rate in vulval induction.

LIN-3 polarity is necessary for precise AC to P6.p alignment

One mechanism ensuring robust vulval induction involves the progressive alignment of P6.p with the AC during the L2 stage (Grimbert et al., 2016). Despite the initial variability in the location of the AC relative to P6.p in wild-type early L2 larvae, the AC and P6.p are precisely

aligned to each other by the early L3 stage. LIN-3 signaling is required for the migration of VPCs towards the AC (Grimbert et al., 2016). Together with lateral LIN-12 NOTCH signaling between the VPCs, which compete for the inductive signal, this results in an almost invariant alignment of the AC with the nearest VPC P6.p (Huelsz-Prince and van Zon, 2017).

We thus investigated whether changes in LIN-3 polarity or in global AC polarity affect the AC to P6.p alignment. For this purpose, we measured the distance between the AC and P6.p, as well as the distance between P6.p and P5.p (or P7.p if the AC was located posterior to P6.p) and calculated the relative P6.p to AC alignment index R (**Fig. 6A,B,H**). In wild-type mid to late L2 and early L3 larvae, R never exceeded a value of 0.4, signifying that the AC was always situated closest to P6.p. In 18% (n=35) of *unc-6(lf)* L2 larvae, R exceeded a value of 0.4, and the AC was occasionally situated equidistant or even closer to P5.p or P7.p (**Fig. 6A**). By the early L3 stage, the AC in *unc-6(lf)* mutants had aligned with P6.p in 90% of the cases (**Fig. 6B**). In *nlp-26(lf)* and *sra-9(lf)* mutants, the defects in AC to P6.p alignment were more subtle. The mean alignment index R was slightly higher and the variability (i.e. variance) of R was increased in *sra-9(lf)* and *nlp-26(lf)* larvae at the mid to late L2 stage compared to wild-type larvae (**Fig. 6A**). By the early L3 stage, the AC and P6.p were properly aligned in all *sra-9(lf)* and most *nlp-26(lf)* larvae (**Fig. 6B**).

We conclude that polarized localization of LIN-3 in the AC is not absolutely required for AC to P6.p alignment, but it increases the fidelity of the process. The increased error rate in vulval induction and the occasional 1° cell fate shifts in *unc-6(lf)*, *sra-9(lf)* and *nlp-26(lf)* mutants may be caused by the less precise AC to P6.p alignment.

LIN-3 polarity is directed towards P6.p

In the course of our analysis, we noticed that the mNGr::LIN-3 distribution in the AC was not only polarized along the dorso-ventral axis, but also biased along the anterior-posterior axis

towards P6.p before the AC and P6.p had completely aligned (**Fig. 6C**). We thus measured the LIN-3 polarity along the anterior-posterior axis, applying the same method as described above for the dorso-ventral polarity index to calculate a P6.p-directed anterior-posterior LIN-3 polarity index I_{AP} (**Fig. 6H**). A P6.p directed polarity index $I_{AP} > 1$ indicates that LIN-3 distribution is biased towards P6.p. We measured I_{AP} in wild-type, *unc-6(lf)*, *sra-9(lf)* and *nlp-26(lf)* mutants between the mid L2 and early L3 stages, before P6.p and the AC had fully aligned (i.e. in animals with $R > 0.09$). In wild-type larvae, the mean P6.p-directed polarity I_{AP} was significantly higher than 1 ($p < 0.0001$), indicating that LIN-3 distribution in the AC is directed towards P6.p (**Fig. 6C,G**). In *sra-9(lf)* and *nlp-26(lf)* mutants, the mean I_{AP} was reduced and did not significantly differ from 1 ($p = 0.23$ for *sra-9(lf)* and $p = 0.16$ for *nlp-26(lf)*). Thus, P6.p-directed LIN-3 polarity is lost in *sra-9(lf)* and *nlp-26(lf)* mutants (**Fig. 6E-G**). Interestingly, the mean I_{AP} in *unc-6(lf)* mutants was significantly higher than 1 ($p < 0.01$) and comparable to the wild-type I_{AP} (**Fig. 6D,G**). Thus, the P6.p-directed LIN-3 polarity in the AC does not depend on *unc-6*. We also tested if the relative distance R between the AC and P6.p correlates with the P6.p-directed LIN-3 polarity I_{AP} . (In those cases where the AC aligned with P5.p or P7.p, we quantified I_{AP} and R relative to these VPCs.) In wild-type larvae, we observed a tendency to increase the P6.p-directed LIN-3 polarity I_{AP} with decreasing AC to P6.p distance R (**Fig. S5A**). Thus, as P6.p approaches the AC LIN-3 localization becomes more polarized towards P6.p. This trend was weaker in *unc-6(lf)* and absent in *sra-9(lf)* and *nlp-26(lf)* mutants (**Fig. S5B-D**).

Our data thus far suggest that during the process of AC alignment, the AC senses the proximity of the nearest VPC and progressively channels LIN-3 secretion into this direction. The perception of the nearest VPC appears to be preserved in *unc-6(lf)* mutants, though the overall efficiency is slightly reduced due to the loss of dorso-ventral AC polarity. On the other hand,

NLP-26 and SRA-9 are required, directly or indirectly, for the communication between the AC and the most proximal VPC to induce the asymmetric distribution of LIN-3.

***nlp-26* is expressed and acts in the VPCs while *sra-9* functions in the AC**

Since *nlp-26* encodes a predicted secreted neuropeptide-like protein, we hypothesized that NLP-26 may constitute a signal secreted by the VPCs or the VNC. The *gfp::nlp-26(zh113)* strain, which carries a *gfp* insertion in place of the signal sequence, did not show any GFP expression, probably because endogenous *nlp-26* expression levels are very low. We thus generated a multi-copy transcriptional *nlp-26* reporter by fusing 1.4 kb of the *nlp-26* 5' regulatory region to an *nls::lacZ::gfp* reporter cassette in order to confine the GFP signal to the nuclei (*zhEx632[P_{nlp-26}-nls::lacZ::gfp]*). This transcriptional *nlp-26* reporter was dynamically expressed in the VPCs and their sister Pn.a neurons in the VNC. In early to mid L2 larvae, *P_{nlp-26}-nls::lacZ::gfp* was expressed in all VPCs and their sister Pn.a neurons (**Fig. 7A**). In addition, *nlp-26* was strongly expressed in the *hyp7* cell at all stages (inset in **Fig. 7A**). By the late L2/early L3 stage, *nlp-26* transcription was up-regulated in P6.p and the P6.a neurons, while expression faded in the other VPCs (**Fig. 7B,C**). *nlp-26* continued to be expressed in the P6.px daughter cells of mid L3 larvae (**Fig. 7D**). Note that the descendants of the 3° VPCs P3.p, P4.p and P8.p began to express *nlp-26* after they had fused with *hyp7* (**Fig. 7D**).

To observe *sra-9* expression, we inserted by CRISPR/Cas9-mediated genome editing a *gfp::3xFlag* cassette in frame at the 3' end of the *sra-9* coding sequences to generate the endogenous *sra-9* reporter (*zh151[sra-9::gfp::loxP::3xFlag]*). In mid L2 larvae, SRA-9::GFP was expressed in the AC and other uterine cells but not in the VPCs or the VNC (**Fig. 7E**). From the early L3 stage on, SRA-9::GFP expression was also observed in the VPCs, while AC expression faded until it was absent in mid-L3 (Pn.px stage) larvae (**Fig. 7F,G**).

The *nlp-26* and *sra-9* expression patterns suggested that NLP-26 might act as a signal secreted by the VPC that polarizes LIN-3 trafficking in the AC, while SRA-9 could function in the AC to transduce the VPC signal. We therefore performed Pn.p cell- and uterine-specific RNAi of *nlp-26* and *sra-9* using the *zhEx418[lin-31::rde-1]* (Haag et al., 2014) and *qyIs102[fos-1ap::rde-1]* (Matus et al., 2010) transgenes, respectively, in the *rrf-3(lf); rde-1(lf)* background, as described in Yang et al. (2017) (**Fig. S6A,B**). We then quantified the polarity of the GFP::LIN-3 reporter in the AC under the different RNAi conditions. Pn.p cell-specific *sra-9* RNAi had no significant effect on GFP::LIN-3 polarity compared to empty vector controls (**Fig. 8A,B,G**), but *nlp-26* RNAi reduced GFP::LIN-3 polarity (**Fig. 8C,G**). Conversely, uterine-specific *sra-9* RNAi reduced LIN-3 polarity, while *nlp-26* RNAi had no significant effect compared to the empty vector controls (**Fig. 8D,E,F,H**). To further define the cellular focus of *sra-9* in the uterus, we expressed wild-type *sra-9* under control of the *lin-3* AC-specific element (Hwang and Sternberg, 2004) together with an mCherry reporter in the *sra-9(lf)* background, using the bi-cistronic transgene *zhIs143[P_{ACEL}>sra-9::SL2::mCherry]* (**Fig. S6C**). AC-specific expression of *sra-9* rescued the GFP::LIN-3 polarity defects of *sra-9(lf)* mutants, suggesting that SRA-9 functions in the AC (**Fig. 8I-L**).

Thus, NLP-26 may act as a feedback signal secreted by the VPCs to polarize via SRA-9 the secretion of LIN-3 by the AC.

Discussion

C. elegans vulval cell fate specification serves as an excellent in vivo model to analyze the subcellular localization of the EGF ligand and receptor at single cell resolution. It has been proposed that the limiting amounts of LIN-3 secreted by the AC form a gradient that can act in a dose-dependent manner to specify the different fates of the proximal VPCs (Katz et al., 1995). Moreover, LET-23 expressed on the basolateral surface of the nearest VPC P6.p sequesters most of the LIN-3 signal (Hajnal et al., 1997) (**Fig. 9A**). If LET-23 is mislocalized to the apical VPC compartment, then less LIN-3 is sequestered by P6.p and the inductive signal can reach the distal VPCs (**Fig. 9B**). Thus, LET-23 localized on the basolateral membrane of P6.p limits the range of the graded LIN-3 signal.

Polarized LIN-3 secretion determines the distribution of the inductive signal

Here, we show that not only LET-23 localization in the VPCs, but also the polarized secretion of LIN-3 by the AC regulates the range of the inductive signal (**Fig. 9C**). Our results indicate that the AC polarizes LIN-3 trafficking from the endoplasmic reticulum towards its ventral side that faces the VPCs. This polarized secretion depends on the global AC polarity established by the ventral to dorsal UNC-6 Netrin gradient (Ziel et al., 2009). LIN-3 secretion is then further enriched in the direction of the nearest VPC, usually P6.p, along the anterior-posterior axis. While dorso-ventral LIN-3 polarity is strongly reduced in *unc-6 netrin(lf)* mutants, the secretion of LIN-3 in the direction of the nearest VPC along the anterior-posterior axis occurs independently of the UNC-6-dependent AC polarity.

Using an unbiased, genome-wide approach, we have identified two genes, *sra-9* and *nlp-26*, that are specifically required for polarized LIN-3 localization and do not affect global AC polarity. *sra-9* encodes an orphan GPCR protein and *nlp-26* a secreted neuropeptide-like protein. *nlp-26* is expressed in the VNC neurons and the VPCs, where it shows a dynamic

expression pattern until the late L2/early L3 stage, when expression becomes up-regulated in the 1° VPC that sequesters the LIN-3 signal. Thus, NLP-26 could act as a secreted cue from the VPCs that polarizes LIN-3 trafficking in the AC. This hypothesis is supported by the finding that Pn.p cell-specific depletion of *nlp-26*, but not of *sra-9*, reduced LIN-3 polarity in the AC. An endogenous *sra-9* reporter was expressed in the AC of mid-L2 larvae, the period when LIN-3 polarity is first observed, and AC-specific expression of *sra-9* rescued the LIN-3 polarity defects of *sra-9(lf)* mutants. Thus, SRA-9 could be required for the transduction of the NLP-26 signal in the AC. Whether SRA-9 functions as a receptor for NLP-26 in the AC remains to be determined. Taken together, SRA-9 and NLP-26 appear to be part of a sensing mechanism used by the AC to detect the location of the nearest VPC and focus LIN-3 secretion into the direction of the future 1° VPC. Since the VPCs migrate towards the AC along a LIN-3 gradient while competing for the inductive AC signal via DELTA/NOTCH-mediated lateral inhibition, AC to P6.p alignment and 1° vulval cell fate specification are tightly coupled (Huelsz-Prince and van Zon, 2017). Our data indicate that the AC plays an active part in this feedback mechanism. We propose that the AC directs and channels LIN-3 secretion towards the “leader” in the race of the VPCs for the 1° cell fate (**Fig. 9A**). As a result, the LIN-3 gradient becomes progressively restricted and the closest VPC, the “winner”, receives most of the inductive signal.

Polarized LIN-3 secretion ensures robust vulval induction

Vulval fate specification is extremely robust. In the wild-type larvae grown under standard conditions, P6.p adopts the 1° fate in 99.9% of the cases and always induces the 2° fate in its neighbors P5.p and P7.p (Braendle and Félix, 2008). Previous studies have shown that this robustness is achieved through the cross-talk between the inductive EGFR/RAS/MAPK and the lateral DELTA/ NOTCH signaling pathways, which results in the almost invariable alignment of the 1° vulval cell P6.p with the AC (Barkoulas et al., 2013; Berset et al., 2001;

Grimbert et al., 2016; Yoo et al., 2004). Here, we show that the polarized and directed secretion of LIN-3 by the AC is an additional mechanism that ensures robust vulval induction. Even though *nlp-26(lf)* and *sra-9(lf)* mutants do not exhibit penetrant vulval phenotypes, they do display at a low penetrance errors in fate patterning, shifts in 1° fate selection and a less precise AC to P6.p alignment. All these defects are probably due to the increased variability in MAPK activation in P6.p we observed using a MPK-1 biosensor. Thus, LIN-3 secretion by the AC is an actively regulated process that depends on the global AC polarity determined by the ventral to dorsal UNC-6 Netrin gradient, and a sensing mechanism to detect the nearest VPC, which is mediated by the neuropeptide-like protein NLP-26 and the GPCR SRA-9 as a candidate receptor. Whether SRA-9 and NLP-26 regulate the secretion of additional proteins by the AC beside LIN-3 remains to be determined. Moreover, *nlp-26(lf)* and *sra-9(lf)* may act in additional tissues besides the VPCs and AC, respectively, and could also affect AC alignment and vulval induction indirectly.

In summary, the directed secretion of a growth factor towards the target tissue may be a common strategy to achieve the robust and efficient patterning of cell fates. Also in mammalian cells, the confined subcellular localization of EGF family ligands regulates the range and directionality of their signaling activity. For example, TGF- α is sorted to the basolateral membrane compartment of epithelial MDCK cells to restrict signal diffusion and promote juxtacrine signaling (Singh and Coffey, 2014). Similarly, Pro-Epiregulin is sorted to the basolateral compartment of MDCK cells, and its mis-localization to the apical compartment causes hyperproliferative, locally invasive tumors (Singh et al., 2013). It will be interesting to investigate if similar feedback mechanisms between signal sending and signal receiving cells are used in the EGF signaling pathway of other species.

Materials and Methods

General methods and strains used

Unless noted otherwise, *C. elegans* strains were maintained at 20 °C on NGM (Nematode Growth Medium) plates applying standard methods (Brenner, 1974). The *C. elegans* Bristol variety N2 was used as wild-type reference, and strains used for the experiments were derivatives of N2. The following alleles and transgenes were used:

LG I: *unc-40(e271)* (Hedgecock et al., 1990), *zhIs127[P_{ACEL Δpes10}>mCherry, unc-119(+)]*,
LG II: *qyls23[P_{cdh-3}::PLCδPH::mCherry, unc-119(+)]* (Ziel et al., 2009), *arTi85[P_{lin-31}::ERK-KTR(NLS3)-mClover-T2A-mCherry-H2B::unc-54 3'UTR, rps-27p::NeoR::unc-54 3'UTR]* (de la Cova et al., 2017), *rrf-3(pk1426)* (Simmer et al., 2002), *let-23(sy1)* (Katz et al., 1996), *ttTi5605* (Frøkjær-Jensen et al., 2008), *sra-9(zh108)* (this study), *sra-9(zh151[sra-9::gfp::loxP::3xFlag])* (this study), LG III: *unc-119(ed3)*, *madd-2(tr103)* (Alexander et al., 2010), *oxTi444*, *zhIs143[P_{ACEL Δpes10}>sra-9_{genomic}::SL2::mCherry::unc-54 3'UTR]*, *unc-119(+)]* (this study), LG IV: *lin-3(e1417)* (Hwang and Sternberg, 2004), *lin-3(zh112[mNGR::loxP::3xFlag])*, LG V: *nlp-26(zh113[gfp::loxP::3xFlag])* (this study), *rde-1(ne219)*, LG X: *unc-6(ev400)* (Hedgecock et al., 1990), *gap-1(ga133)* (Hajnal et al., 1997), unknown LG: *zhIs67[gfp::lin-3, unc-119(+)]* (this study), *qyls102[fos-1ap::rde-1;myo2::yfp; unc-119]* (Matus et al., 2010). Extrachromosomal arrays: *zhEx418[lin-31::rde-1, myo2-mcherry]* (Haag et al., 2014), *zhEx632[P_{nlp-26-nls}::lacZ::gfp, myo2-mcherry]* (this study), *zhEx668.1* to *zhEx668.3[P_{cdh-3}::unc-40_{minigene}::gfp::unc-54 3'UTR]* (this study).

Plasmid construction

DNA fragments were isolated by PCR using templates and primers described in **supplementary Materials and Methods** and assembled using Gibson recombinase (Gibson et al., 2009) or by ligation of restriction fragments.

CRISPR/CAS9-generated alleles

mNGr::lin-3(zh112): To insert the *mNGr::3xFlag* sequence in the 5' region of the *lin-3* locus, the CRISPR/Cas9 system according to (Dickinson et al., 2015) was applied. The repair template plasmid pLM5 was injected at a concentration of 8 ng/μl, the two single guides with integrated CAS9 plasmids pLM12 and pLM13 at a concentration of 40 ng/μl together with the recommended co-injection markers pGH8 (Addgene 19359) at 10 ng/μl, pCFJ104 (Addgene 19328) at 5 ng/μl and pCFJ90 (Addgene 19327) at 2.5 ng/μl.

gfp::nlp-26(zh113): To insert the *gfp::3xFlag* sequence in the 5' region of the *nlp-26* locus, the repair template plasmid pLM7 was injected at a concentration of 10 ng/μl, the three single guide with integrated CAS9 plasmids pLM8, pLM9 and pLM10 at a concentration of 50 ng/μl together with the same co-injection markers used for *zh112*.

The *sra-9(zh108)* deletion allele was generated according to the Arribere et al. (2014) protocol, with following single guide sequences: TTG GCA AAG TTC TAG TTA T, AC C AAT TGA ATT GCT GGA T.

sra-9::gfp(zh151): To insert a *gfp::3xFlag* cassette into the 3' region of the *sra-9* locus, the repair template plasmid pSS22 was injected at a concentration of 10 ng/μl, the two single guide with integrated CAS9 plasmids pSS20 and pSS21 at a concentration of 50 ng/μl together with the with the same co-injection markers used for *zh112*.

Selection of homologous integrands was done according to the protocol by Dickinson et al. (2015).

RNA interference

RNA interference (RNAi) was performed using the feeding method as described by Kamath and Ahringer (2003). P0 worms were synchronized at the L1 stage, transferred to NGM plates

containing 3 mM IPTG and 50 ng/ml ampicillin seeded with the indicated RNAi bacteria and allowed to grow for 5-7 days at 20°C, after which the F1 progeny was analyzed. For Pn.p cell-specific RNAi, a strain of the genotype *rrf-3(pk1426)II; unc-119(ed4)III; rde-1(ne219)V; zhEx418[lin-31::rde-1; myo2-mcherry]* including the *zhIs67[gfp::lin-3, unc-119(+)]* reporter was used and LIN-3 polarity was measured in the F1 generation in three independent experiments. To control the tissue specificity of this RNAi strain, we performed global and Pn.p cell-specific *lin-3* RNAi and observed expression of the *zhIs67* reporter (**Fig. S6**). For uterine-specific RNAi, a strain of the genotype *rrf-3(pk1426)II; unc-119(ed4)III; rde-1(ne219)V; qyls102[fos-1ap::rde-1; myo-2::yfp]* including the *zhIs67[gfp::lin-3, unc-119(+)]* reporter was used and LIN-3 polarity was measured in the F1 generation in three independent experiments.

Microscopy and image analysis

Images were acquired using an Olympus BX61 wide-field microscope equipped with a Cr.E.S.T. X-light spinning disc system, a Lumencor SPECTRA X light engine and a Hamamatsu Orca CMOS camera or an iXon Ultra 888 EMCCD camera controlled by the Visitron VisiView 2.1.1 software. Fluorescent image z-stacks of the mNGr::LIN-3 and GFP::LIN-3 reporters were processed using the Huygens Deconvolution software (SVI, Center for Microscopy and Image Analysis, University of Zürich). Images were analyzed with Fiji/ImageJ software (Schindelin et al., 2012).

Determination of the developmental stage

The developmental stages were determined by measuring the gonad length in Nomarski images, as described (Kimble and Hirsh, 1979), and animals were divided into three groups; the early

to mid L2 stage (gonad: 30-70 μm), the late L2 stage (gonad: 70-110 μm) and the early to mid L3 stage (gonad: 110-150 μm).

AC polarity measurements

The dorso-ventral and anterior-posterior AC polarity for LIN-3 and PIP_2 was measured using a semi-automated script in Fiji creating summed z-projections of image stacks across the AC with 0.2 to 0.14 μm z-spacing with prior deconvolution (for LIN-3::mNGR and GFP::LIN-3) or in which the background had been subtracted (for *P_{cdh3}::mCherry::PLC δ^{PH}*). A threshold was applied to set pixel intensities outside of the AC to zero. The dorso-ventral polarity index I_{DV} was calculated by dividing the AC into equal areas of the ventral and dorsal halves defined by the center of the AC nucleus in the DIC image and dividing the average ventral signal intensity by the average dorsal intensity. Thus, an $I_{DV} > 1$ indicates a higher signal intensity in the ventral half of the AC. An analogous method was used to calculate the P6.p-directed LIN-3 polarity index I_{AP} by dividing the AC into equal halves proximal and distal to P6.p or to the nearest VPC, as shown in **Fig. 6H**.

Vulval induction counts

Vulval induction was scored by examining worms at the L4 stage under Nomarski optics as described in (Sternberg and Horvitz, 1986). The number of VPCs that had adopted a 1° or 2° vulval cell fate was counted for each animal, and the vulval induction index (VI) was calculated by dividing the total number of induced cells by the number of animals scored. Animals with a $VI > 3$ were scored as hyper-induced, and animals with $VI < 3$ as hypo-induced. The different strains combinations compared in the vulval induction assays were generated from progeny obtained in the same crosses.

AC to P6.p alignment

For the alignment quantification, the distance between the AC and either P6.p or the closest VPC was measured as illustrated in **Fig. 6H**. To calculate the relative alignment index R, this value was divided by the P6.p to P5.p or to P7.p distance depending on the AC location.

ERK-nKTR biosensor quantification

MPK-1 activity in the VPCs was measured using the recently established ERK-nKTR biosensor *arTi85*, which is based on the MPK-1 activity-dependent nuclear export of the biosensor (de la Cova et al., 2017). Custom-made ImageJ (Schindelin et al., 2012) and Cell Profiler (Carpenter et al., 2006) scripts were used to process and quantify the images taken in the indicated mutant backgrounds under standardized illumination conditions, as described in Maxeiner et al. (2019). Flat field illumination and background corrections were done using blank and dark field images, respectively, taken for each experiment. The nuclear red/green (mCherry::H2B/ nKTR::mClover) average intensity ratios were measured in each VPC (except for P3.p) in summed z-projections of the five central slices taken with a z-spacing of 0.13 μm , relative to the focus of the nuclear mCherry::H2B signal. Since we could not assume that P4.p was not affected, the red/green nuclear ratio for each VPC was normalized to the average of the red/green ratios in P4.p-P8.p in the same animal, rather than normalizing to the ratio in P4.p, as described by de la Cova et al. (2017). The normalized values are plotted in **Fig. 5 F-I**.

Statistical analysis

Statistical analyses for vulval induction (VI) was performed by bootstrapping the data with a resample size of 10'000 samples. The standard deviation within the bootstrapped samples was used to estimate the standard error of the mean and the 95% confidence interval. Statistical analysis of continuous measures (I_{DV} , I_{AP} , R) was performed using Student's t-tests or Fisher's exact tests as indicated in the figure legends.

Acknowledgements

We wish to thank the members of the Hajnal laboratory, Esther Stöckli, Markus Affolter and Stefan Luschnig for critical discussion and comments on the manuscript. We are also grateful to Gino Poulin and the Hengartner laboratory for technical support, the *C. elegans* Genetic Center for providing strains, Andrew Fire for GFP vectors and J. Ahringer for RNAi clones. This work was supported by a grant from the Swiss National Science Foundation to A.H. no. 31003A-166580 and the Kanton of Zürich.

Author contributions

L.M., M.M, S.S., J.M.E, P.G., M.D and M.W. performed the experiments; L.M. and A.H. analyzed the data and wrote the manuscript.

References

- Alexander, M., Selman, G., Seetharaman, A., Chan, K. K. M., D'souza, S. A., Byrne, A. B. and Roy, P. J.** (2010). MADD-2, a homolog of the Opitz syndrome protein MID1, regulates guidance to the midline through UNC-40 in *Caenorhabditis elegans*. **18**, 961–972.
- Arribere, J. A., Bell, R. T., Fu, B. X., Artiles, K. L., Hartman, P. S. and Fire, A. Z.** (2014). Efficient Marker-Free Recovery of Custom Genetic Modifications with CRISPR/Cas9 in *Caenorhabditis elegans*. *Genetics*.
- Barkoulas, M., van Zon, J. S., Milloz, J., Van Oudenaarden, A. and Félix, M.-A.** (2013). Robustness and epistasis in the *C. elegans* vulval signaling network revealed by pathway dosage modulation. **24**, 64–75.
- Berset, T., Hoier, E. F., Battu, G., Canevascini, S. and Hajnal, A.** (2001). Notch inhibition of RAS signaling through MAP kinase phosphatase LIP-1 during *C. elegans* vulval development. *Science* **291**, 1055–1058.
- Braendle, C. and Félix, M.-A.** (2008). Plasticity and errors of a robust developmental system in different environments. **15**, 714–724.
- Brenner, S.** (1974). The genetics of *Caenorhabditis elegans*. *Genetics* **77**, 71–94.
- Carpenter, A. E., Jones, T. R., Lamprecht, M. R., Clarke, C., Kang, I. H., Friman, O., Guertin, D. A., Chang, J. H., Lindquist, R. A., Moffat, J., et al.** (2006). CellProfiler: image analysis software for identifying and quantifying cell phenotypes. *Genome Biol* **7**, R100.
- Chen, N. and Greenwald, I.** (2004). The lateral signal for LIN-12/Notch in *C. elegans* vulval development comprises redundant secreted and transmembrane DSL proteins. **6**, 183–192.
- Dempsey, P. J., Meise, K. S., Yoshitake, Y., Nishikawa, K. and Coffey, R. J.** (1997). Apical enrichment of human EGF precursor in Madin-Darby canine kidney cells involves preferential basolateral ectodomain cleavage sensitive to a metalloprotease inhibitor. *J Cell Biol* **138**, 747–758.
- Dickinson, D. J., Pani, A. M., Heppert, J. K., Higgins, C. D. and Goldstein, B.** (2015). Streamlined Genome Engineering with a Self-Excising Drug Selection Cassette. *Genetics* **200**, 1035–1049.
- Dutt, A., Canevascini, S., Froehli-Hoier, E. and Hajnal, A.** (2004). EGF signal propagation during *C. elegans* vulval development mediated by ROM-1 rhomboid. *PLoS Biol* **2**, e334.
- Estes, K. A. and Hanna-Rose, W.** (2009). The anchor cell initiates dorsal lumen formation during *C. elegans* vulval tubulogenesis. *Dev Biol* **328**, 297–304.
- Félix, M.-A. and Barkoulas, M.** (2012). Robustness and flexibility in nematode vulva development. *Trends in Genetics* **28**, 185–195.
- Frøkjær-Jensen, C., Davis, M. W., Hopkins, C. E., Newman, B. J., Thummel, J. M., Olesen, S.-P., Grunnet, M. and Jorgensen, E. M.** (2008). Single-copy insertion of transgenes in *Caenorhabditis elegans*. **40**, 1375–1383.

- Gibson, D. G., Young, L., Chuang, R.-Y., Venter, J. C., Hutchison, C. A. and Smith, H. O.** (2009). Enzymatic assembly of DNA molecules up to several hundred kilobases. *Nat Meth* **6**, 343–345.
- Greenwald, I. and Kovall, R.** (2013). Notch signaling: genetics and structure. *WormBook* 1–28.
- Grimbert, S., Tietze, K., Barkoulas, M., Sternberg, P. W., Félix, M.-A. and Braendle, C.** (2016). Anchor cell signaling and vulval precursor cell positioning establish a reproducible spatial context during *C. elegans* vulval induction. *Dev Biol* **416**, 123–135.
- Haag, A., Gutierrez, P., Bühler, A., Walser, M., Yang, Q., Langouët, M., Kradolfer, D., Fröhli, E., Herrmann, C. J., Hajnal, A., et al.** (2014). An In Vivo EGF Receptor Localization Screen in *C. elegans* Identifies the Ezrin Homolog ERM-1 as a Temporal Regulator of Signaling. *PLoS Genet* **10**, e1004341.
- Hajnal, A., Whitfield, C. W. and Kim, S. K.** (1997). Inhibition of *Caenorhabditis elegans* vulval induction by gap-1 and by let-23 receptor tyrosine kinase. **11**, 2715–2728.
- Hedgecock, E. M., Culotti, J. G. and Hall, D. H.** (1990). The unc-5, unc-6, and unc-40 genes guide circumferential migrations of pioneer axons and mesodermal cells on the epidermis in *C. elegans*. *Neuron* **4**, 61–85.
- Hill, R. J. and Sternberg, P. W.** (1992). The gene lin-3 encodes an inductive signal for vulval development in *C. elegans*. **358**, 470–476.
- Hoskins, R., Hajnal, A. F., Harp, S. A. and Kim, S. K.** (1996). The *C. elegans* vulval induction gene lin-2 encodes a member of the MAGUK family of cell junction proteins. **122**, 97–111.
- Huelsz-Prince, G. and van Zon, J. S.** (2017). Canalization of *C. elegans* Vulva Induction against Anatomical Variability. *Cell systems* **4**, 219–230.e6.
- Hwang, B. J. and Sternberg, P. W.** (2004). A cell-specific enhancer that specifies lin-3 expression in the *C. elegans* anchor cell for vulval development. **131**, 143–151.
- Hynes, N. E. and MacDonald, G.** (2009). ErbB receptors and signaling pathways in cancer. *Curr Opin Cell Biol* **21**, 177–184.
- Iwamoto, R., Handa, K. and Mekada, E.** (1999). Contact-dependent growth inhibition and apoptosis of epidermal growth factor (EGF) receptor-expressing cells by the membrane-anchored form of heparin-binding EGF-like growth factor. *J Biol Chem* **274**, 25906–25912.
- Kaech, S. M., Whitfield, C. W. and Kim, S. K.** (1998). The LIN-2/LIN-7/LIN-10 complex mediates basolateral membrane localization of the *C. elegans* EGF receptor LET-23 in vulval epithelial cells. *Cell* **94**, 761–771.
- Kamath, R. S. and Ahringer, J.** (2003). Genome-wide RNAi screening in *Caenorhabditis elegans*. *Methods* **30**, 313–321.
- Katz, W. S., Hill, R. J., Clandinin, T. R. and Sternberg, P. W.** (1995). Different levels of the *C. elegans* growth factor LIN-3 promote distinct vulval precursor fates. *Cell* **82**, 297–307.

- Katz, W. S., Lesa, G. M., Yannoukakos, D., Clandinin, T. R., Schlessinger, J. and Sternberg, P. W.** (1996). A point mutation in the extracellular domain activates LET-23, the *Caenorhabditis elegans* epidermal growth factor receptor homolog. *Mol Cell Biol* **16**, 529–537.
- Kimble, J.** (1981). Alterations in cell lineage following laser ablation of cells in the somatic gonad of *Caenorhabditis elegans*. *Dev Biol* **87**, 286–300.
- Kimble, J. and Hirsh, D.** (1979). The postembryonic cell lineages of the hermaphrodite and male gonads in *Caenorhabditis elegans*. *Dev Biol* **70**, 396–417.
- de la Cova, de, C., Townley, R., Regot, S. and Greenwald, I.** (2017). A Real-Time Biosensor for ERK Activity Reveals Signaling Dynamics during *C. elegans* Cell Fate Specification. *Dev. Cell* **42**, 542–553.e4.
- Massagué, J. and Pandiella, A.** (1993). Membrane-anchored growth factors. *Annual review of biochemistry* **62**, 515–541.
- Matus, D. Q., Li, X. Y., Durbin, S., Agarwal, D., Chi, Q., Weiss, S. J. and Sherwood, D. R.** (2010). In Vivo Identification of Regulators of Cell Invasion Across Basement Membranes. *Science Signaling* **3**, ra35–ra35.
- Maxeiner, S., Grolleman, J., Schmid, T., Kammenga, J. and Hajnal, A.** (2019). The hypoxia-response pathway modulates RAS/MAPK-mediated cell fate decisions in *Caenorhabditis elegans*. *Life Sci Alliance* **2**, e201800255.
- Morf, M. K., Rimann, I., Alexander, M., Roy, P. and Hajnal, A.** (2013). The *Caenorhabditis elegans* homolog of the Opitz syndrome gene, *madd-2/Mid1*, regulates anchor cell invasion during vulval development. *Dev Biol* **374**, 108–114.
- Nathoo, A. N., Moeller, R. A., Westlund, B. A. and Hart, A. C.** (2001). Identification of neuropeptide-like protein gene families in *Caenorhabditis elegans* and other species. **98**, 14000–14005.
- Schindelin, J., Arganda-Carreras, I., Frise, E., Kaynig, V., Longair, M., Pietzsch, T., Preibisch, S., Rueden, C., Saalfeld, S., Schmid, B., et al.** (2012). Fiji: an open-source platform for biological-image analysis. *Nat Meth* **9**, 676–682.
- Simmer, F., Tijsterman, M., Parrish, S., Koushika, S. P., Nonet, M. L., Fire, A., Ahringer, J. and Plasterk, R. H. A.** (2002). Loss of the putative RNA-directed RNA polymerase RRF-3 makes *C. elegans* hypersensitive to RNAi. *Curr. Biol.* **12**, 1317–1319.
- Simske, J. S. and Kim, S. K.** (1995). Sequential signalling during *Caenorhabditis elegans* vulval induction. **375**, 142–146.
- Singh, B. and Coffey, R. J.** (2014). Trafficking of Epidermal Growth Factor Receptor Ligands in Polarized Epithelial Cells. *Annual Review of Physiology* **76**, 275–300.
- Singh, B., Bogatcheva, G., Washington, M. K. and Coffey, R. J.** (2013). Transformation of polarized epithelial cells by apical mistrafficking of epiregulin. *Proceedings of the National Academy of Sciences* **110**, 8960–8965.

- Sorkin, A. and Goh, L. K.** (2008). Endocytosis and intracellular trafficking of ErbBs. *Exp Cell Res* **314**, 3093–3106.
- Sternberg, P. W.** (2005). Vulval development. *WormBook* 1–28.
- Sternberg, P. W. and Horvitz, H. R.** (1986). Pattern formation during vulval development in *C. elegans*. *Cell* **44**, 761–772.
- Sundaram, M. V.** (2013). Canonical RTK-Ras-ERK signaling and related alternative pathways. *WormBook* 1–38.
- Troemel, E. R., Chou, J. H., Dwyer, N. D., Colbert, H. A. and Bargmann, C. I.** (1995). Divergent seven transmembrane receptors are candidate chemosensory receptors in *C. elegans*. *Cell* **83**, 207–218.
- Urban, S., Lee, J. R. and Freeman, M.** (2001). *Drosophila* rhomboid-1 defines a family of putative intramembrane serine proteases. *Cell* **107**, 173–182.
- Whitfield, C. W., Bénard, C., Barnes, T., Hekimi, S. and Kim, S. K.** (1999). Basolateral localization of the *Caenorhabditis elegans* epidermal growth factor receptor in epithelial cells by the PDZ protein LIN-10. *Mol Biol Cell* **10**, 2087–2100.
- Wyckoff, J., Wang, W., Lin, E. Y., Wang, Y., Pixley, F., Stanley, E. R., Graf, T., Pollard, J. W., Segall, J. and Condeelis, J.** (2004). A paracrine loop between tumor cells and macrophages is required for tumor cell migration in mammary tumors. *Cancer Res* **64**, 7022–7029.
- Yang, Q., Roiz, D., Mereu, L., Daube, M. and Hajnal, A.** (2017). The Invading Anchor Cell Induces Lateral Membrane Constriction during Vulval Lumen Morphogenesis in *C. elegans*. *Dev. Cell* **42**, 271–285.e3.
- Yogev, S., Schejter, E. D. and Shilo, B.-Z.** (2010). Polarized secretion of *Drosophila* EGFR ligand from photoreceptor neurons is controlled by ER localization of the ligand-processing machinery. *PLoS Biol* **8**, e1000505.
- Yoo, A. S., Bais, C. and Greenwald, I.** (2004). Crosstalk between the EGFR and LIN-12/Notch pathways in *C. elegans* vulval development. *Science* **303**, 663–666.
- Ziel, J. W., Hagedorn, E. J., Audhya, A. and Sherwood, D. R.** (2009). UNC-6 (netrin) orients the invasive membrane of the anchor cell in *C. elegans*. *Nat Cell Biol* **11**, 183–189.

Figures

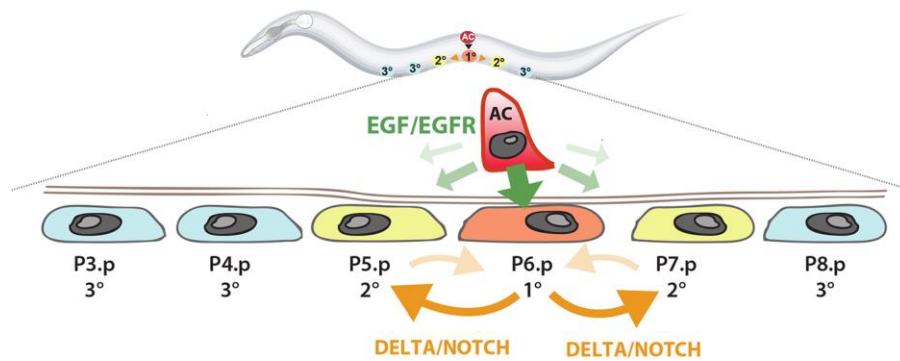


Figure 1. Model of vulval development.

The AC releases LIN-3 to induce the 1° cell fate in the most proximal VPC P6.p. The lateral DELTA signal from P6.p specifies the 2° fate in the adjacent VPCs P5.p and P7.p, while the distal VPCs P3.p, P4.p and P8.p adopt the uninduced 3° fate.

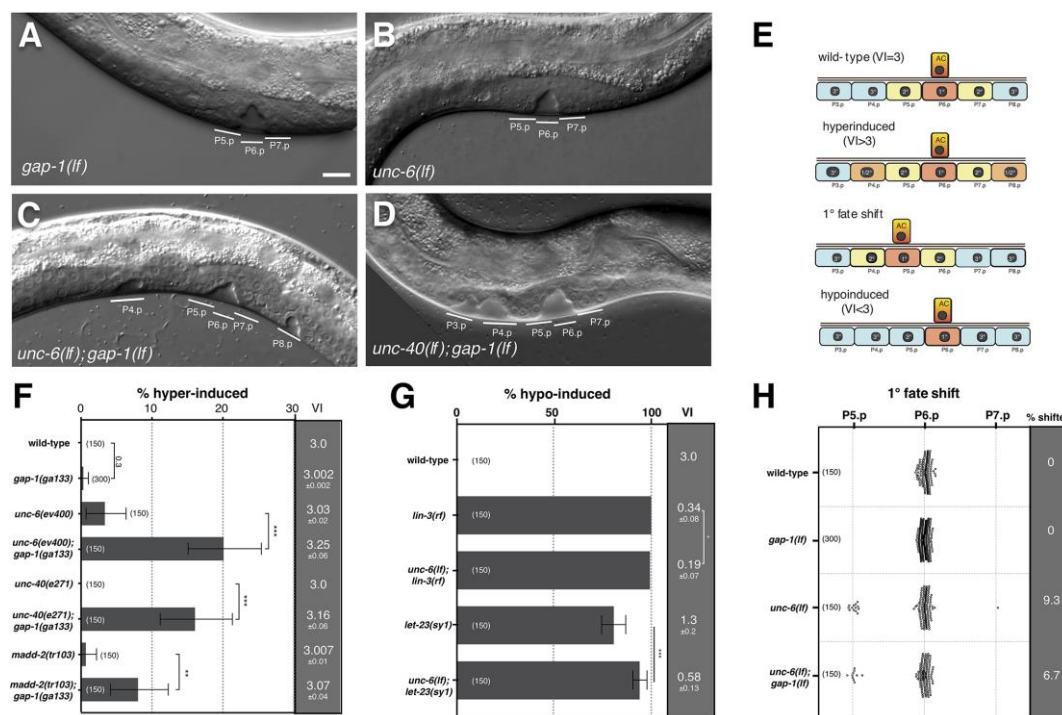


Figure 2. AC polarity is necessary for robust vulval induction.

(A-D) Nomarski images of mid L4 stage larvae of the indicated genotypes. The white lines indicate the descendants of induced VPCs that formed an invagination. The scale bar in (A) is 10 μ m. (E) Schematic drawing illustrating the different observed vulval phenotypes; wild-type (VI=3), hyper-induced (VI>3), 1° fate shift, and hypo-induced (VI<3). (F) The percentages of animals with a hyper-induced vulval phenotype (VI>3) are shown for the indicated genotypes. The gray column to the right shows the average VI \pm standard error of the mean. (G) The percentages of animals with a hypo-induced vulval phenotype (VI<3) are shown for the indicated genotypes. The gray column to the right shows the average VI \pm standard error of the mean. (H) Animals with a 1° cell fate shift from P6.p to P5.p or P7.p. For each genotype, the percentage of animals showing a 1° fate shift is shown in the gray column to the right. The error bars in (F) and (G) indicate the 95% confidence intervals calculated by bootstrapping with a resampling size of 10'000. p-values were calculated with a t-test for independent samples and are indicated as p < 0.05 = *, p < 0.01 = ** and p < 0.001 = ***. The numbers in brackets in each plot refer to the numbers of animals scored.

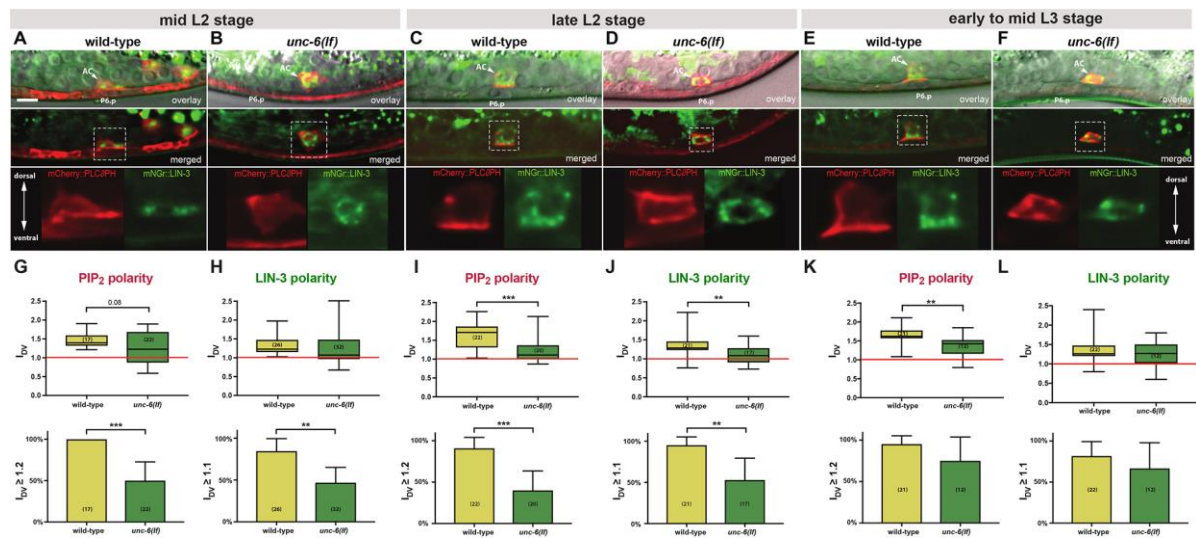


Figure 3. LIN-3 expression in the AC is polarized and requires the UNC-6 Netrin signal.

(A) Top row: Nomarski images of a mid-sagittal plane overlaid with summed z-projections of the *P_{cdh3}::mCherry::PLCδ^{PH}* (red) and the *mNGR::lin-3* (green) reporters in wild-type and (B) *unc-6(lf)* mid L2 larvae. The positions of the AC (arrowheads) and the P6.p nuclei are indicated. The middle row shows the merged z-projections of the *P_{cdh3}::mCherry::PLCδ^{PH}* (red) and the *mNGR::lin-3* (green) reporters alone. The dashed boxes outline the AC regions magnified about 2.5-fold in the bottom row. The scale bar in (A) is 5 μm. (C) Reporter expression in wild-type and (D) *unc-6(lf)* late L2 and (E, F) early to mid L3 larvae. Animals were staged according to their gonad length as described in the materials and methods section. (G) Box plots of the PIP₂ (*mCherry::PLCδ^{PH}*) and (H) the LIN-3 polarity indices *I_{DV}* in wild-type and *unc-6(lf)* mid-L2 larvae. Error bars indicate the min and max values, and statistical significance was calculated with a t-test for independent samples of unequal variance (p < 0.05 = *, p < 0.01 = ** and p < 0.001 = ***). See materials and methods for details on the quantification. The graphs underneath the box plots show the percentages of animals with a PIP₂ *I_{DV}* > 1.2 and a LIN-3 *I_{DV}* > 1.1. These threshold values correspond approximately to the 10th percentile for the two markers. Error bars indicate the 95% confidence intervals. Statistical significance was calculated using the nonparametric, unpaired Man-Whitney test (p < 0.05 = *, p < 0.01 = ** and p < 0.001 = ***).

$p < 0.001 = ***$). (I,J) show the same analysis for late L2 and (K,L) for early to mid L3 larvae.

The numbers in brackets in each graph refer to the numbers of animals scored for each genotype and stage.

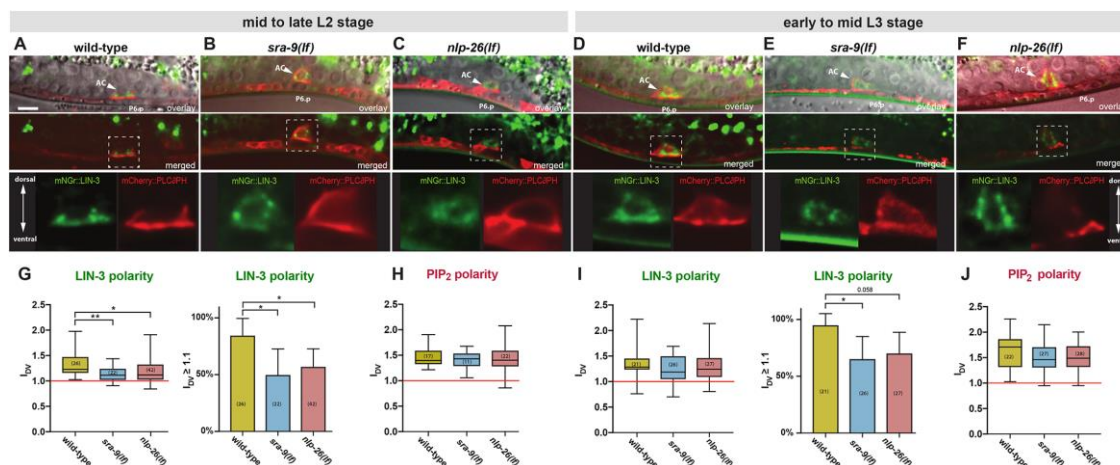


Figure 4. SRA-9 and NLP-26 are required for LIN-3 polarity but not for global AC polarity.

(A) Top row: Nomarski images of a mid-sagittal plane overlaid with summed z-projections of the $P_{cdh3}::mCherry::PLC\delta^{PH}$ (red) and the $mNGr::lin-3$ (green) reporters in wild-type, (B) *sra-9(lf)* and (C) *nlp-26(lf)* mid to late-L2 larvae. The positions of the AC (arrowheads) and the P6.p nuclei are indicated. The middle row shows the merged z-projections of the $P_{cdh3}::mCherry::PLC\delta^{PH}$ (red) and the $mNGr::lin-3$ (green) reporters alone. The dashed boxes outline the AC regions magnified about 2.5-fold in the bottom row. The scale bar in (A) is 5 μ m. (D) Reporter expression in wild-type, (E) *sra-9(lf)* and (F) *nlp-26(lf)* early to mid L3 larvae. Animals were staged according to their gonad length as described in the materials and methods section. (G) Box plots of the LIN-3 and (H) PIP₂ ($mCherry::PLC\delta^{PH}$) polarity indices I_{DV} in wild-type, *sra-9(lf)* and *nlp-26(lf)* larvae at the mid to late L2 stage and (I), (J) at the early to mid L3 stage. Error bars indicate the min and max values, and statistical significance was calculated with a t-test for independent samples of unequal variance ($p < 0.05 = *$ and $p < 0.01 = **$). The graphs beside the box plots in (G) and (I) show the percentages of animals with a LIN-3 $I_{DV} > 1.1$. Error bars indicate the 95% confidence intervals. Statistical significance was calculated using the nonparametric, unpaired Man-Whitney test ($p < 0.05 = *$ and $p < 0.01 = **$). The numbers in brackets in each graph refer to the numbers of animals scored for each genotype and stage.

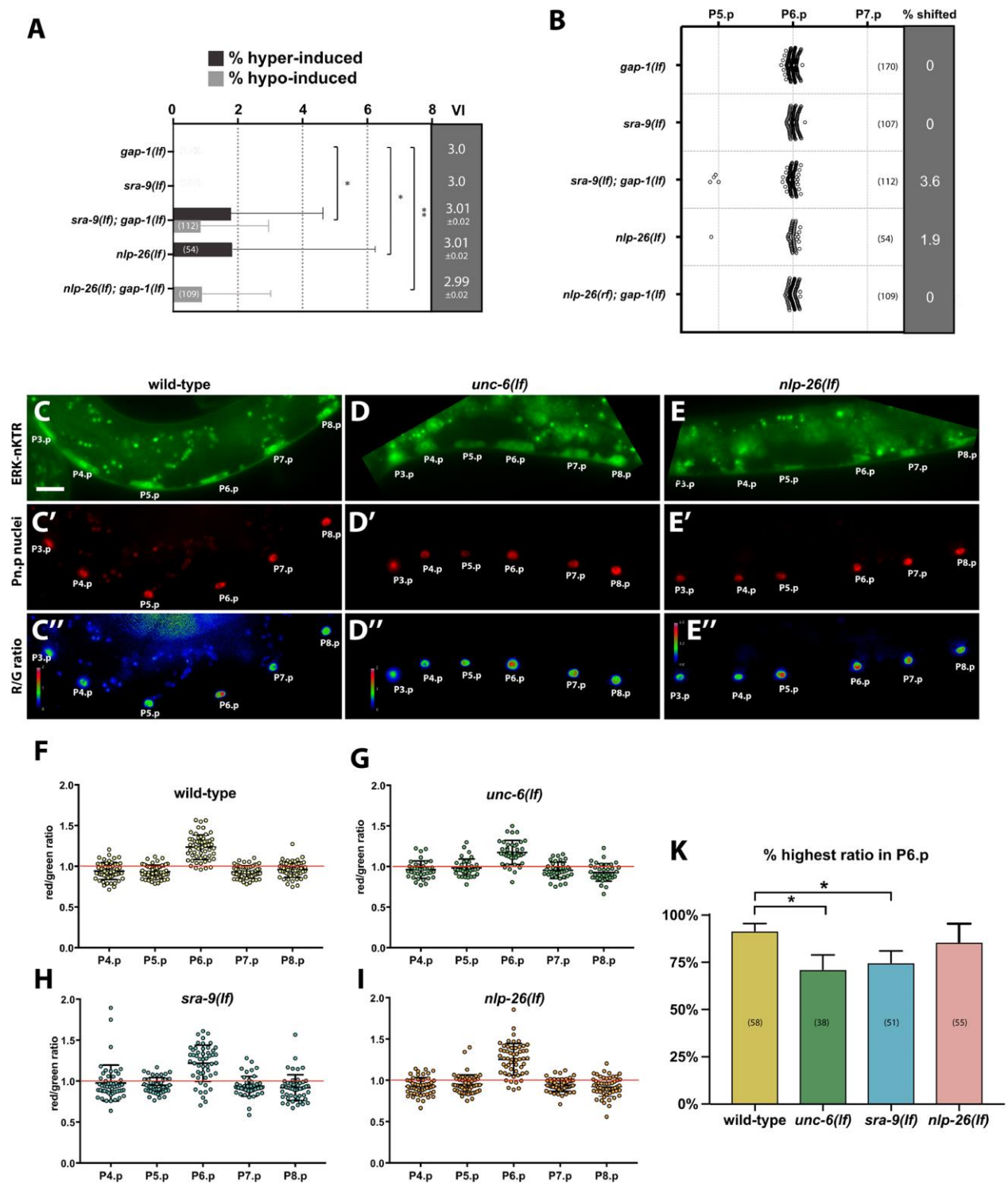


Figure 5. *sra-9(lf)* and *nlp-26(lf)* mutants exhibit an increased error rate in vulval fate specification and higher variability in MPK-1 activation.

(A) The percentages of animals with hyper-induced (dark gray) or hypo-induced (light gray) vulval phenotypes are shown for the indicated genotypes. The gray column to the right shows

the average VI \pm standard error of the mean. (B) Animals with 1° cell fate shifts. For each genotype, the percentage of animals showing a 1° fate shift is shown in the gray column to the right. (C-C'') ERK-nKTR biosensor activity in the VPCs of wild-type, (D-D'') *unc-6(lf)* and (E-E'') *nlp-26(lf)* mid L2 larvae. The top row shows the ERK-nKTR::mClover signal in green, the middle row the mCherry::H2B reference in red and the bottom row the red/green ratio images. Note in (E'') the relatively higher activity in P5.p than in P6.p. The scale bar in (C) is 5 μ m. (F) ERK-nKTR biosensor activity levels plotted as red/green intensity ratios in the VPCs of wild-type, (G) *unc-6(lf)*, (H) *sra-9(lf)* and (I) *nlp-26(lf)* mid L2 larvae. (K) Percentages of animals exhibiting highest biosensor activity in P6.p. The error bars show the 95% confidence intervals calculated by bootstrapping with a resampling size of 10'000. p-values were calculated in (A) with a t-test for independent samples and in (K) with the nonparametric, unpaired Man-Whitney test are indicated as $p < 0.05 = *$ and $p < 0.01 = **$. The numbers in brackets in each plot refer to the numbers of animals scored.

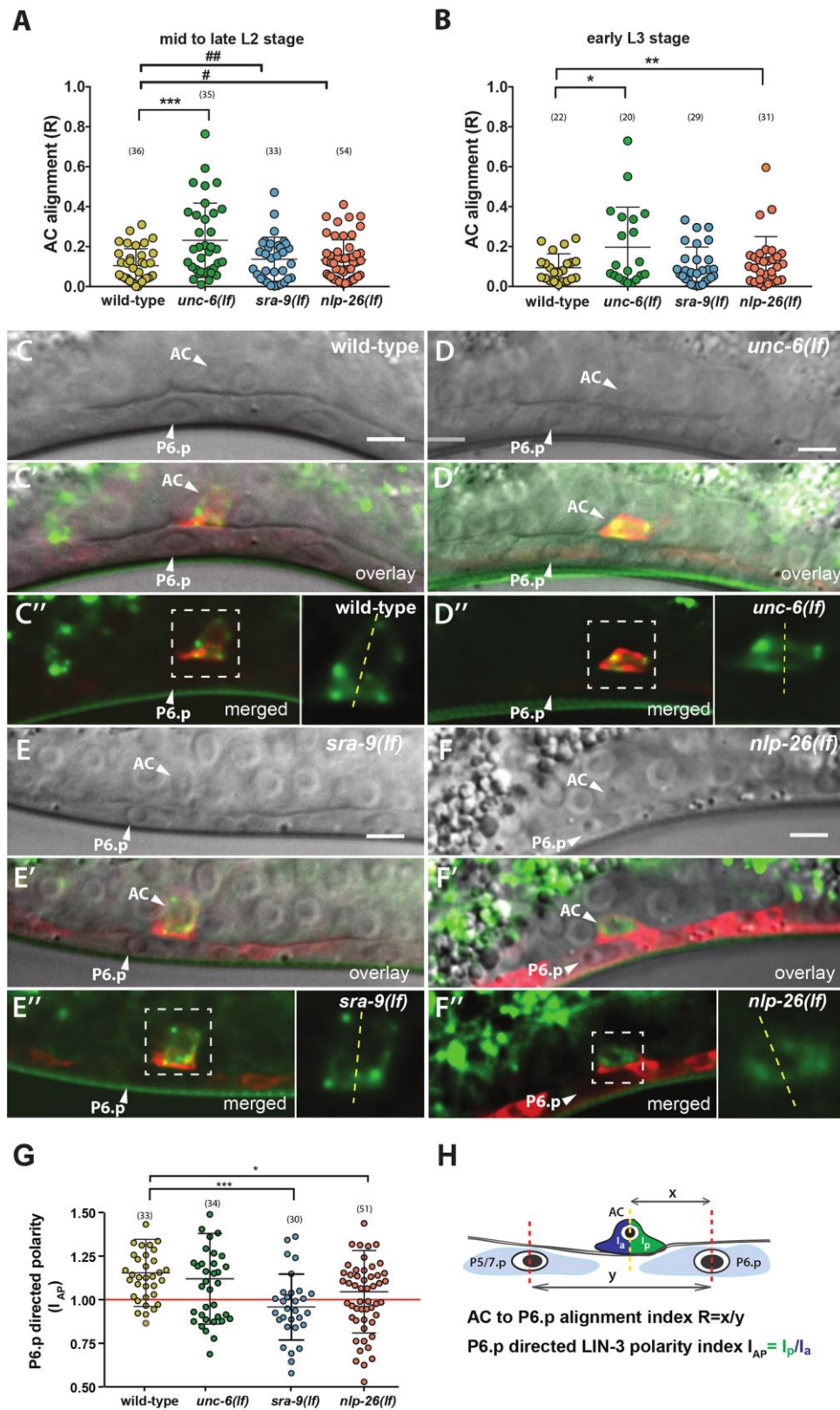


Figure 6. SRA-9 and NLP-26 are required for efficient AC to P6.p alignment and P6.p-directed LIN-3 polarity.

(A) AC to P6.p alignment indices R in mid to late L2 and (B) early L3 larvae of the indicated genotypes. A t-test for independent samples and equal variance was used to determine the statistical significant differences between the wild-type and mutants at each developmental stage. ($p < 0.05 = *$, $p < 0.01 = **$ and $p < 0.001 = ***$). # indicate the results of an F-test for variance, which indicates differences in the range of the measured values ($p < 0.05 = \#$ and $p < 0.01 = \#\#$). (C) Nomarski images of a mid-sagittal plane, (C') overlaid with summed z-projections of the *P_{cdh3}::mCherry::PLC δ^{PH}* (red) and the *mNGr::lin-3* (green) signals and (C'') merged z-projections in a wild-type, (D-D'') an *unc-6(lf)*, (E-E'') a *sra-9(lf)* and (F-F'') an *nlp-26(lf)* mid-L2 larva. The AC and the P6.p nuclei are labelled with arrowheads. The insets in (C'', D'', E'' & F'') show approximately 2.5-fold magnifications of the ACs in the regions outlined by the dashed boxes. The dashed yellow lines in the insets indicate the border between the anterior and posterior halves of the AC that were measured to calculate the P6.p-directed LIN-3 polarity index I_{AP} , as illustrated in (H). The scale bars are 5 μ m. Note in (C'') the wild-type and (D'') the *unc-6(lf)* mutant the enrichment of mNGr::LIN-3 in the anterior half of the AC facing P6.p. (E'') In the AC of the *sra-9(lf)* and (F'') the *nlp-26(lf)* mutants, mNGr::LIN-3 is more uniformly distributed along the anterior-posterior axis. (G) P6.p-directed LIN-3 polarity indices I_{AP} for animals of the indicated genotypes with a relative alignment index R greater than 0.09 (i.e. before complete AC to P6.p alignment when P6.p-directed secretion can be observed). A t-test for independent samples was used to determine statistical significance ($p < 0.05 = *$ and $p < 0.001 = ***$). (H) Schematic illustration of the measurements taken to calculate the relative AC to P6.p alignment index (R) and the P6.p-directed LIN-3 polarity index (I_{AP}).

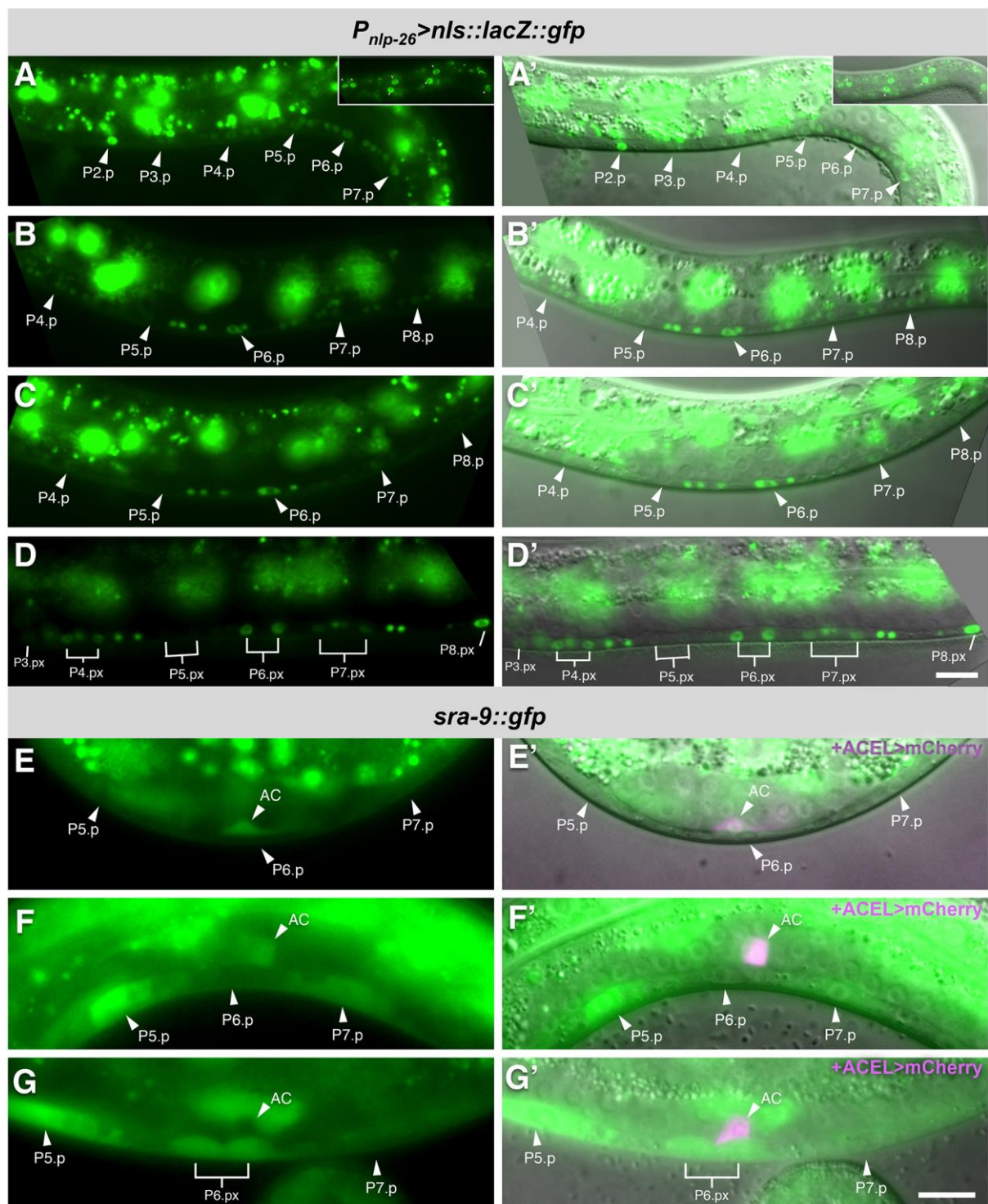


Figure 7. *nlp-26* is expressed in the VPCs and *sra-9* in the AC of L2 larvae.

(A) *P_{nlp-26}>nls::lacZ::gfp* reporter expression in the VPCs and Pn.a neurons of an early L2 larva
 (A') overlay with the corresponding Nomarski image. The insets in the upper right show a top layer with some of the hyp7 nuclei expressing the *P_{nlp-26}-nls::lacZ::gfp* reporter. (B,B') Expression

in mid L2 and (C,C') late L2/early L3 larva. (D,D') *nlp-26* reporter expression in the VPC descendants at the Pn.px stage in a late L3 larva. Note in (D), the relatively strong expression in the 3° P4.p and P8.p descendants after they had fused with hyp7. (E) Endogenous SRA-9::GFP expression in the AC of a mid L2 larva, (E') merged with the AC marker *zhls127[ACEL>mCherry]* in magenta and overlaid on the corresponding Nomarski image. (F, F') SRA-9::GFP expression in the AC as well as in P5.p & P7.p at the early L3 stage, and (G, G') in the P6.px cells after the first round of VPC divisions at the mid-L3 stage. No more AC expression of SRA-9::GFP was detected from the mid-L3 stage on. The arrowheads point at the VPC and AC nuclei and the lines in (D) and (G) at the VPC descendants. The scale bars in (D') and (G') are 10 μ m.

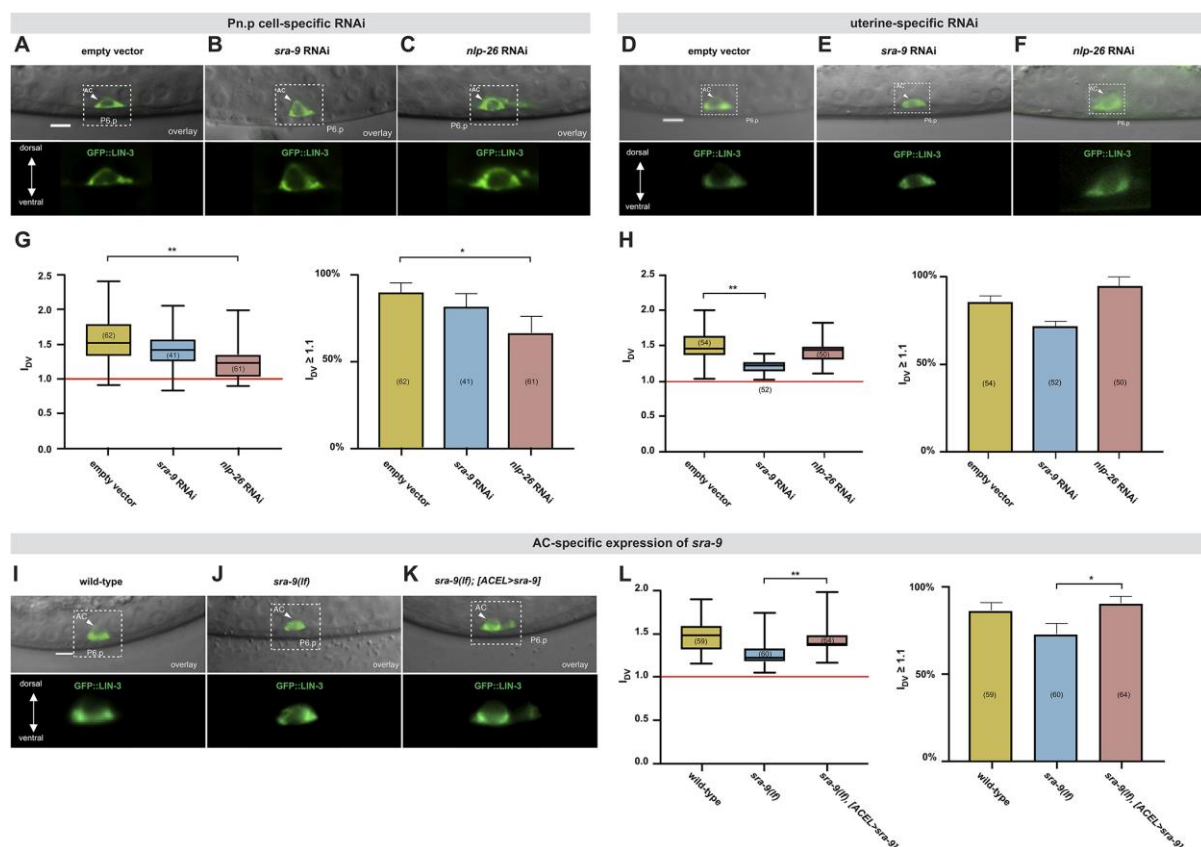


Figure 8. *nlp-26* acts in the Pn.p cells and *sra-9* in the AC.

(A) Top rows: Nomarski images of a mid-sagittal plane overlaid with the GFP::LIN-3 reporter expression (green) after Pn.p cell-specific RNAi in an empty vector control, (B) *sra-9* RNAi and (C) *nlp-26* RNAi animal at the mid-L2 stage. (D) GFP::LIN-3 reporter expression after uterine-specific RNAi in an empty vector control, (E) *sra-9* RNAi (F) *nlp-26* RNAi animal at the mid-L2 stage. The position of the AC (arrowheads) and the P6.p nuclei are indicated. The dashed boxes outline the AC regions magnified about 2.5-fold in the bottom rows. (G) Box plots of the LIN-3 polarity index I_{DV} after Pn.p cell-specific RNAi and (H) after uterine-specific RNAi quantified at the mid-L2 stage. (I) Top rows: Nomarski images of a mid-sagittal plane overlaid with the GFP::LIN-3 (green) reporter signal in a wild-type control, (J) a *sra-9(zh108lf)* mutant and (K) a *sra-9(zh108lf)* mutant carrying the AC-specific *zhIs143[P_{ACEL}>*sra-9::SL2::mCherry*]* rescue construct. (L) Box plot of the LIN-3 polarity index I_{DV} in the wild-

type, *sra-9(zh108lf)* and the *sra-9(zh108lf); zhIs143[P_{ACEL}>sra-9::SL2::mCherry]* background. The bar graphs to the right of each box plot show the percentages of animals with a LIN-3 I_{DV} >1.1. Error bars in the box plots indicate the min and max values, and statistical significance was calculated with a t-test for independent samples of unequal variance ($p < 0.01 = **$). Error bars in the bar graphs indicate the 95% confidence intervals, and statistical significance was calculated using the nonparametric, unpaired Man-Whitney test ($p < 0.05 = *$ and $p < 0.01 = **$). The numbers in brackets refer to the numbers of animals scored for each condition. The scale bars in (A), (D) and (I) are 5 μm .

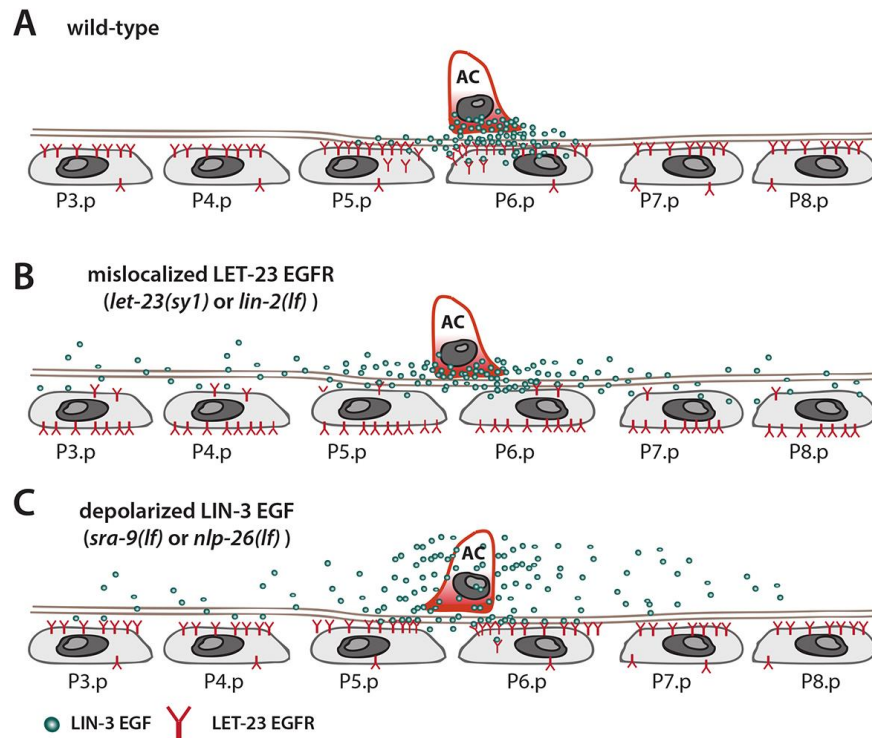


Figure 9. Model for polarized LIN-3 secretion.

(A) In the wild-type, the limiting amounts of LIN-3 secreted by the AC are efficiently sequestered by an excess of LET-23 on the basolateral side of P6.p to prevent the spreading of the signal to distal VPCs. (B) The *let-23(sy1)* mutation causes the mislocalization of LET-23 from the basolateral to the apical side of the VPCs. Therefore, LIN-3 is no longer sequestered by LET-23 in P6.p, and the inductive signal can spread to the distal VPCs. The distal VPCs are induced to differentiate if the RAS/MAPK is simultaneously hyperactivated, for example by the *gap-1(lf)* mutation. (C) De-polarization of LIN-3 in the AC, for example in *sra-9(lf)* or *nlp-26(lf)* mutants, likewise results in reduced ligand sequestering by P6.p and the spreading of LIN-3 to more distal VPCs.

Supplementary information

Supplementary Table S1

cellular function	gene	WB identifier	brief description	LIN-3 polarity	AC polarity
cell adhesion					
	<i>dig-1</i>	WBGene00000998	immunoglobulin superfamily	P	n.d.
cell cycle					
	<i>cdk-4</i>	WBGene00000406	cyclin-dependent serine/threonine protein kinase	P	n.d.
	<i>cki-1</i>	WBGene00000516	cyclin-dependent kinase inhibitor p27	P	n.d.
	<i>cye-1</i>	WBGene00000871	E-type cyclin	n.d.	n.d.
	<i>cdk-11.1</i>	WBGene00015203	cyclin-dependent serine/threonine protein kinase	P	n.d.
	<i>cdk-2</i>	WBGene00019362	cyclin-dependent serine/threonine protein kinase	P	n.d.
cell signaling					
	<i>lag-2</i>	WBGene00002246	DSL family NOTCH ligand	P	n.d.
	<i>nlp-26</i>	WBGene00003764	predicted neuropeptide	D	P
	<i>sra-9</i>	WBGene00005035	G-protein coupled receptor	D	P
	<i>srd-36</i>	WBGene00005114	G-protein coupled receptor	P	n.d.
	<i>srh-8</i>	WBGene00005234	G-protein coupled receptor	P	n.d.
	<i>srh-247</i>	WBGene00005453	G-protein coupled receptor	D	P
	<i>unc-40</i>	WBGene00006776	netrin receptor	D	D
	<i>unc-73</i>	WBGene00006805	guanine nucleotide exchange factor similar to Trio	n.d.	n.d.
	<i>madd-2</i>	WBGene00016539	C1 subfamily of tripartite motif (TRIM) protein	D	D
	<i>toe-2</i>	WBGene00016971	DEP domain containing protein	P	n.d.
cellular iron ion homeostasis					
	Y45F10D.4	WBGene00012885	iron-sulfur cluster assembly enzyme	P	n.d.
chromosome organization					
	<i>dpy-27</i>	WBGene00001086	SMC4 subunit of mitotic condensin	P	n.d.
	<i>his-72</i>	WBGene00001946	H3 histone	P	n.d.
	<i>hmg-3</i>	WBGene00001973	Subunit of the heterodimeric FACT complex	P	n.d.
immunity					
	F26F12.5	WBGene00017836	antimicrobial protein	P	
ion transport					
	<i>acr-3</i>	WBGene00000043	nicotinic acetylcholine receptor superfamily	P	n.d.
	<i>mca-1</i>	WBGene00003151	plasma membrane Ca2+ ATPases	P	n.d.
lipid transport					
	<i>cav-2</i>	WBGene00000302	caveolin	P	n.d.
	<i>acbp-3</i>	WBGene00009818	acyl-CoA-binding binding domain	D	D
protein modification					
	<i>usp-48</i>	WBGene00009267	ubiquitin specific peptidase	D	D
	<i>ugt-14</i>	WBGene00019233	UDP glycosyltransferase	P	n.d.
	<i>gei-17</i>	WBGene00001574	SUMO E3 ligase	D	D
	<i>ulp-1</i>	WBGene00006736	SUMO protease	D	D
regulation of transcription					
	<i>lin-1</i>	WBGene00002990	Ets-domain transcription factor	P	n.d.
	<i>lin-9</i>	WBGene00002998	novel protein	P	n.d.
	<i>lin-14</i>	WBGene00003003	novel protein	P	n.d.
	<i>mes-6</i>	WBGene00003224	Polycomb-like chromatin repressive complex	P	n.d.
	<i>nhr-103</i>	WBGene00003693	nuclear hormone receptors	P	n.d.
	<i>nhr-115</i>	WBGene00003705	nuclear hormone receptors	P	n.d.
	<i>sdh-2</i>	WBGene00004746	component of dosage compensation complex	P	n.d.
	<i>sem-4</i>	WBGene00004773	zinc-finger transcription factor	P	n.d.
	<i>din-1</i>	WBGene00008549	spen family transcriptional repressor	P	n.d.
	<i>hpo-11</i>	WBGene00010427	nuclear receptor binding protein 2	P	n.d.
regulation of translation					
	<i>fbf-2</i>	WBGene00001402	Pumilio and FBF family translational regulator	D	D
	<i>puf-8</i>	WBGene00004244	Pumilio and FBF family translational regulator	n.d.	n.d.
small molecule metabolic process					
	<i>cah-4</i>	WBGene00000282	carbonic anhydrase	D	D
	<i>lact-9</i>	WBGene00012890	beta-lactamase domain-containing protein	P	n.d.
	T22F3.3	WBGene00020696	glycogen phosphorylase isozymes	P	n.d.
unknown functions					
	C31H5.5	WBGene00007856	novel protein	n.d.	n.d.
	<i>clec-197</i>	WBGene00008202	C-type lectin	P	n.d.
	T18D3.1	WBGene00011820	novel protein	P	n.d.
	Y69H2.3	WBGene00013481	novel protein	P	n.d.
	ZK795.2	WBGene00014082	novel protein	P	n.d.
	T20D4.11	WBGene00020617	novel protein	P	n.d.
	T02B11.9	WBGene00044777	novel protein	D	D

Table S1. Top 51 candidate genes identified in a whole-genome RNAi screen.

List of 51 genes that reproducibly showed a Muv phenotype in the primary RNAi screen and in four rounds of rescreening. The candidates are grouped into categories of cellular functions. During the re-screening, global AC polarity using the *P_{cdh3}::mCherry::PLC δ^{PH}* (PIP₂) reporter *qyls23* and LIN-3 polarity using the GFP::LIN-3 reporter *zhIs67* were scored simultaneously. P stands for normally polarized and D for defective polarity. In some cases (n. d.), the polarity could not be determined or PIP₂ polarity was not scored because LIN-3 polarity was normal. The three genes, in which RNAi lead to depolarization of GFP::LIN-3 but had no effect on global AC polarity are highlighted in orange. Previously known regulators of AC polarity and positioning that were identified in the screen are highlighted in green.

Supplementary Figures

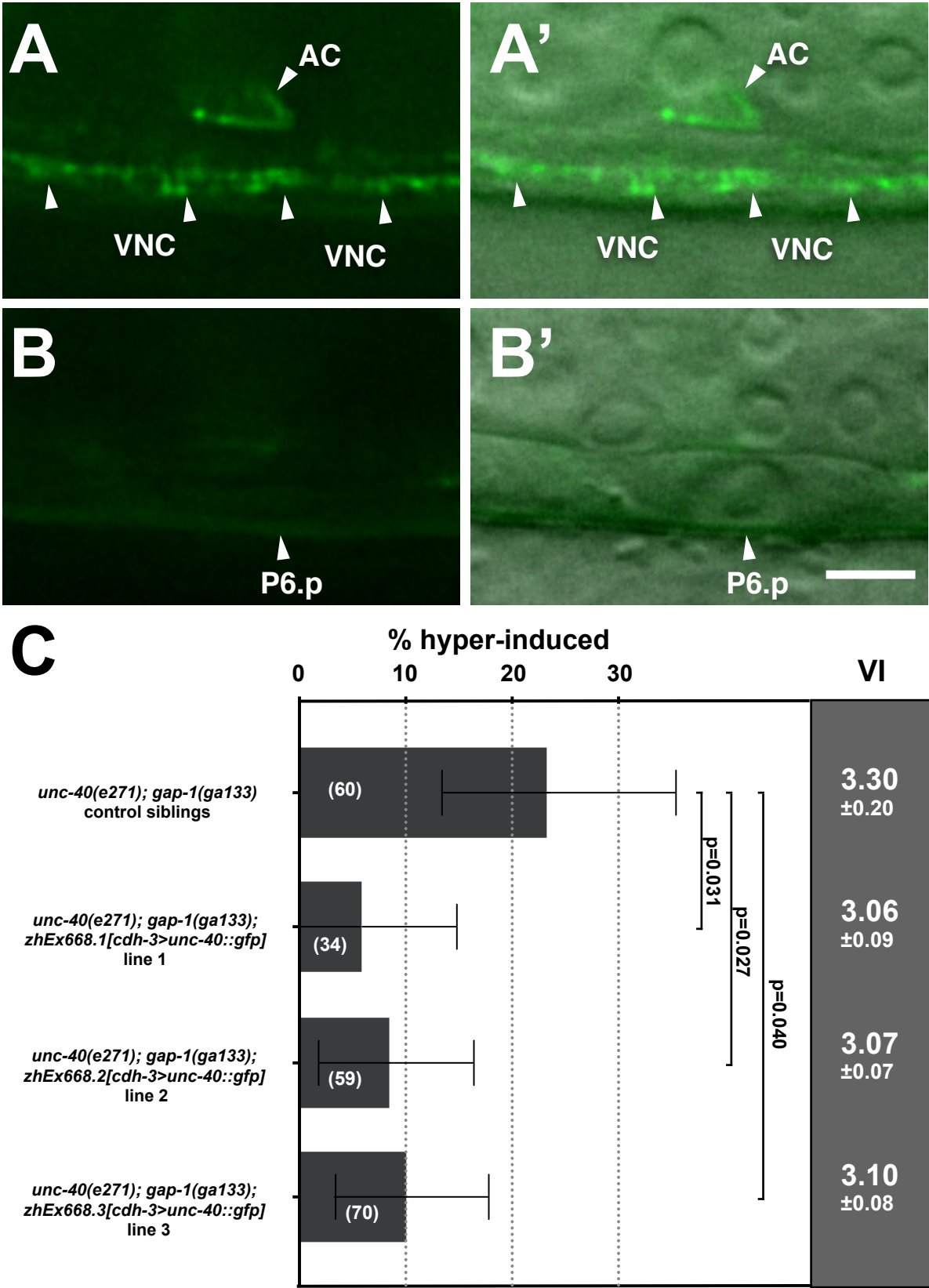


Figure S1. Expression of *unc-40::gfp* in the AC partially rescues the hyper-induced *unc-40(e271); gap-1(ga133)* phenotype.

(A) Expression of the *cdh-3>unc-40::gfp* transgene in the AC and VNC neurons of an early L3 larva, (A') overlaid on the corresponding Nomarski image. (B,B') show a focal plane of P6.p in the same animal. The scale bar in (B') is 5 μ m. (C) The percentages of animals with a hyper-induced vulval phenotype (VI>3) are shown for the three transgenic lines and control siblings lacking the transgene. The gray column to the right shows the average VI \pm standard error of the mean. The error bars indicate the 95% confidence intervals calculated by bootstrapping with a resampling size of 10'000. p-values were calculated with a t-test for independent samples. The numbers in brackets in each plot refer to the numbers of animals scored.

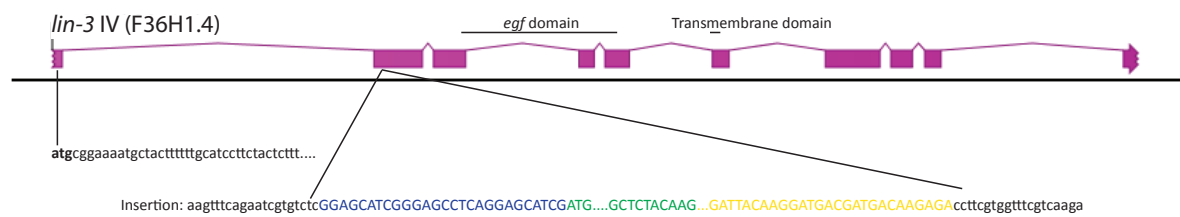


Figure S2. Insertion of the mNGr reporter into the *lin-3* locus (*zh112*).

The sequences are color coded as follows: black: genomic *lin-3* sequences with the initiation codon highlighted in bold; blue: linker sequence; green: mNGr cassette; yellow: 3xFlag tag.

In the *zhIs67* strain, a *gfp* cassette was inserted in place of mNGr.

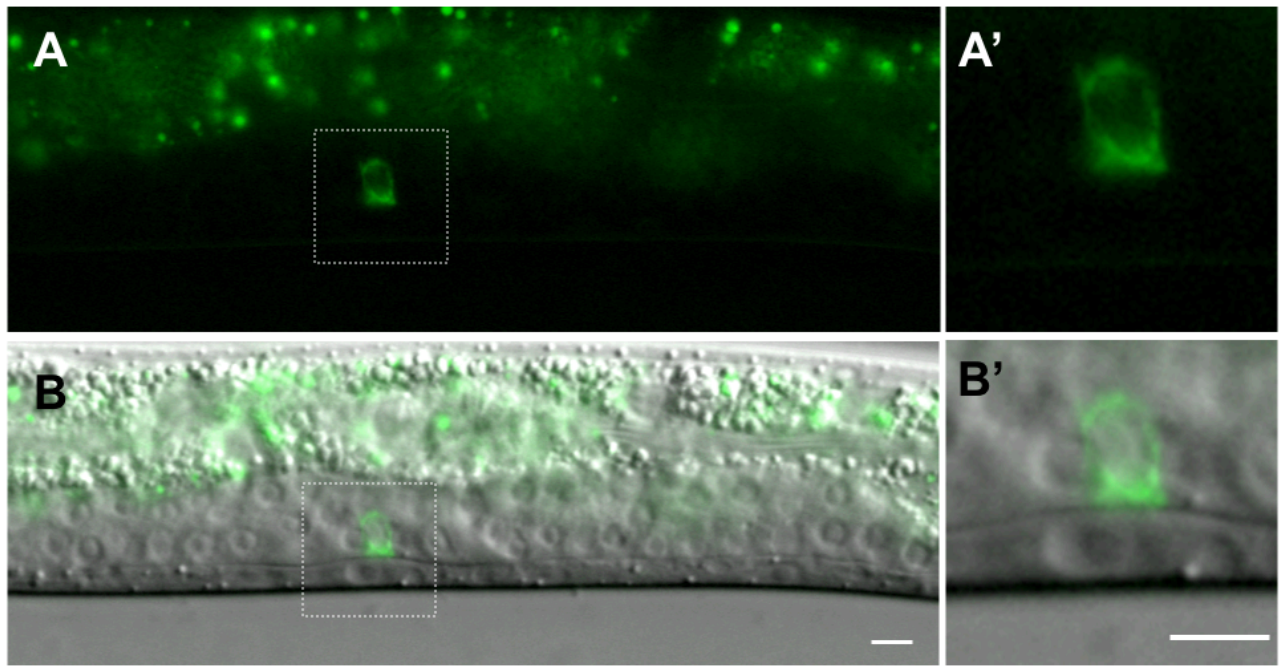


Figure S3. Localization of a multi-copy GFP::LIN-3 transgenic reporter.

(A) Polarized GFP::LIN-3 expression in the AC and (B) merged with the Nomarski image of a late L2 larva using the multi-copy transgene *zhIs67*. The dashed boxes indicate the regions shown enlarged in (A') and (B'). The scale bars are 5 μ m.

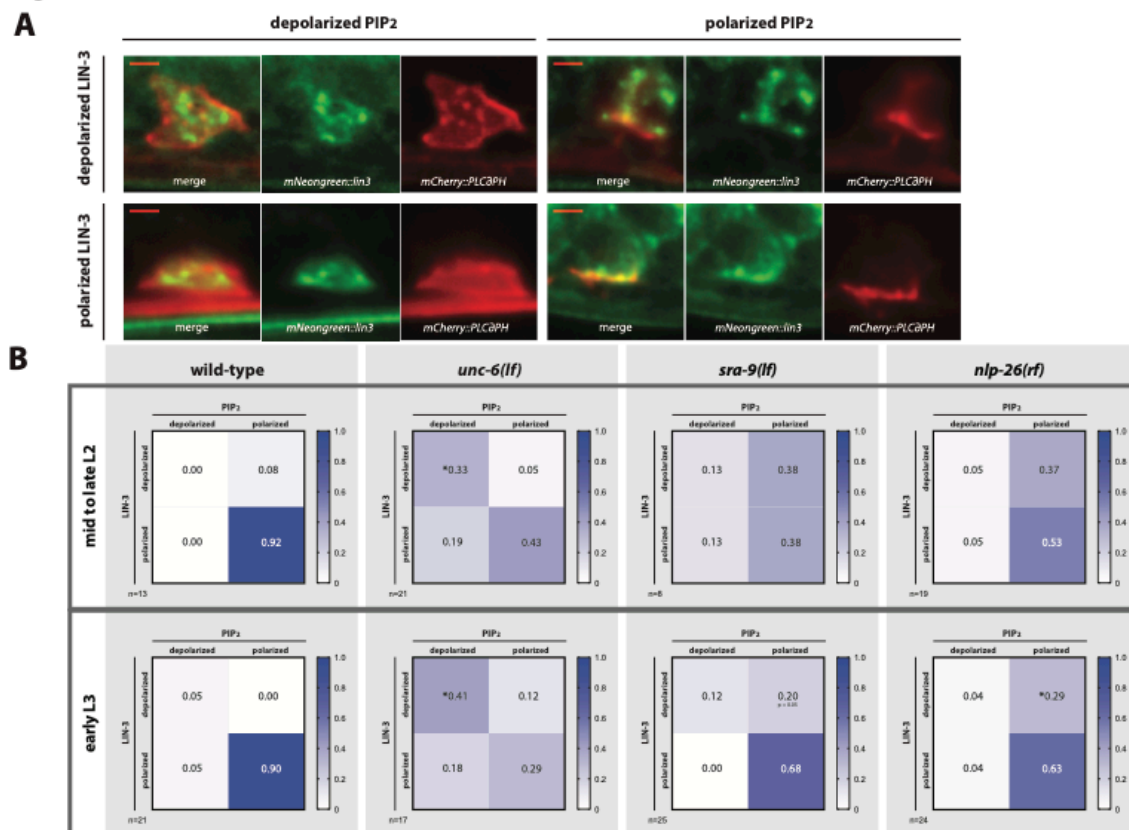


Figure S4. Correlation between global PIP₂ and specific LIN-3 EGF polarity at the single animal level. (A) Examples of summed z-projections of ACs expressing *P_{cdh3}::mCherry::PLC δ^{PH}* PIP₂ marker (red) and the endogenous *mNGr::lin-3* reporter (green) with merged panels to the left depicting the different combinations of polarity observed with the two reporters. The scale bar is 2.5 μ m. (B) Heat-maps showing the correlation between LIN-3 and PIP₂ polarity for wild-type, *unc-6(lf)*, *sra-9(zh108)* and *nlp-26(zh113)* mutants at the mid to late L2 and the early L3 larval stages. Sample size n is indicated for each heat map. LIN-3 was scored as polarized for a I_{DV} > 1.1. A threshold value of PIP₂ I_{DV} > 1.2 was scored as polarized since the mean I_{DV} for the PIP₂ *P_{cdh3}::mCherry::PLC δ^{PH}* reporter in the wild-type was higher than the mean LIN-3 I_{DV}. Statistical significance was calculated with Fisher's exact probability test, (p < 0.05 = * and p < 0.01 = **).

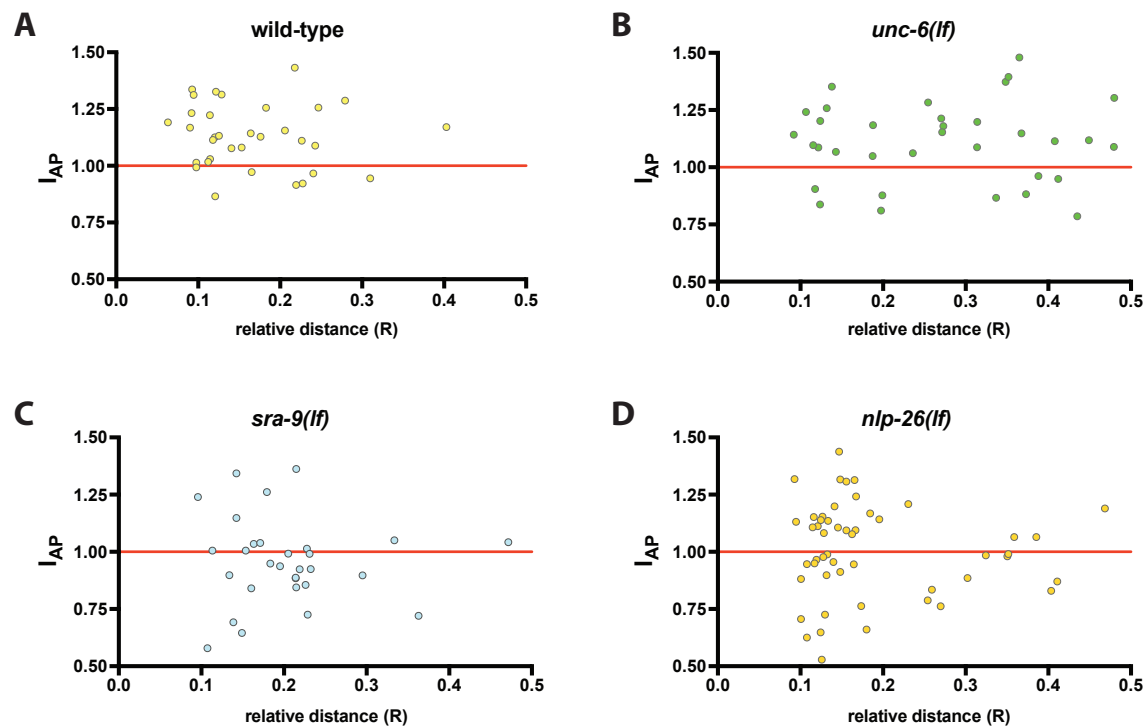


Figure S5. Correlation between the AC to VPC alignment index (R) and VPC-directed LIN-3 polarity (I_{AP}). (A-D) Plots of the VPC-directed LIN-3 polarity index I_{AP} against the relative distance R between AC and the nearest VPC for the indicated genotypes.

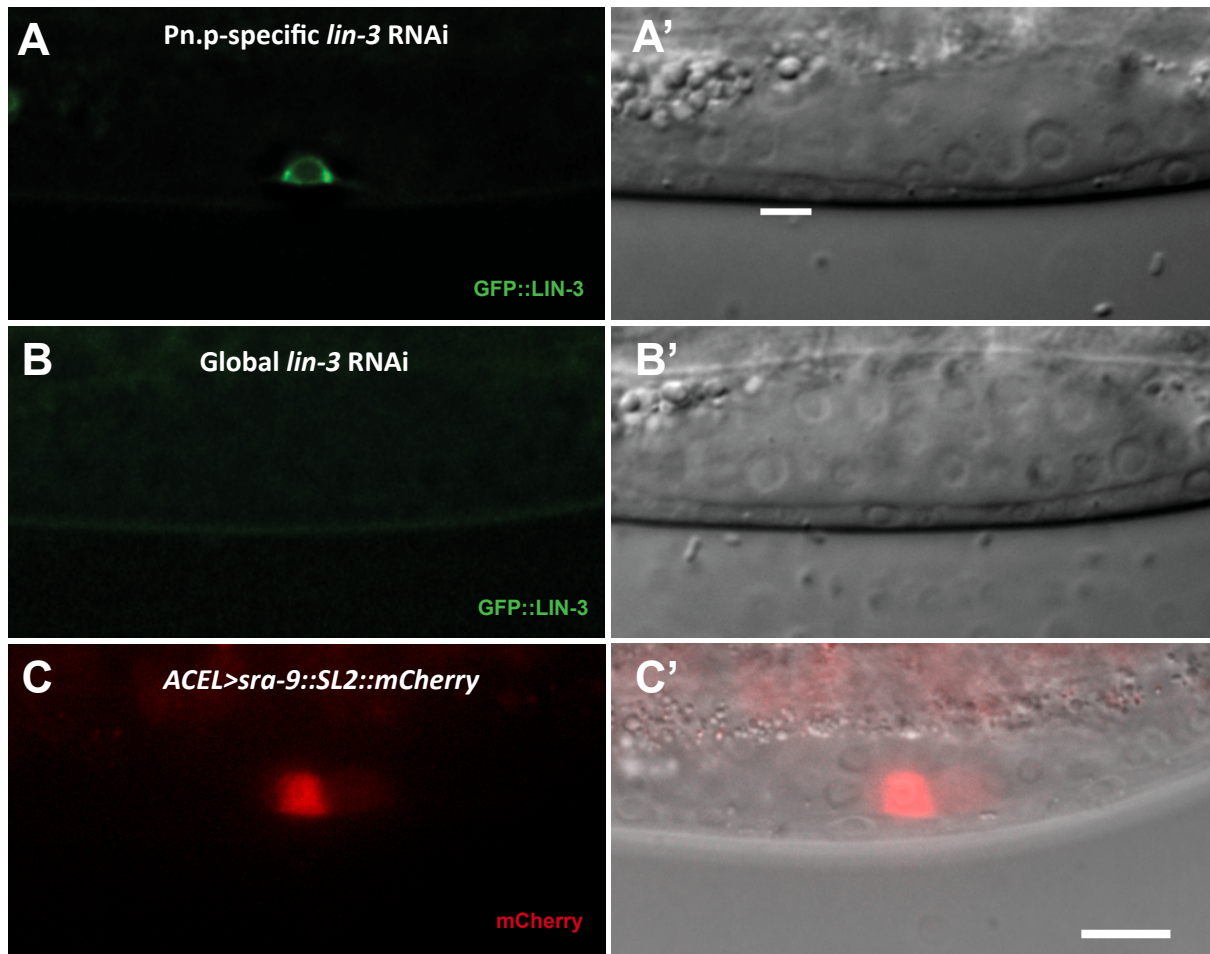


Figure S6. Specificity of the Pn.p-specific RNAi and the AC-specific rescue strains.

(A,A') To monitor the specificity of the tissue-specific RNAi experiment, *lin-3* RNAi was performed in the tissue-specific RNAi strain *rrf-3(pk1426)II; unc-119(ed4)III; rde-1(ne219)V; zhEx418[lin-31::rde-1genomic; myo2-mcherry]; zhIs67[gfp::lin-3, unc-119(+)]*, which permits efficient gene knock-down in the Pn.p cells ((Yang et al., 2017) and (B,B') in the global RNAi strain *rrf-3(pk1426)II; unc-119(ed4)III; zhIs67[gfp::lin-3, unc-119(+)]*. Global *lin-3* RNAi caused the depletion of the GFP::LIN-3 signal in the AC and a Vul phenotype, while Pn.p cell-specific RNAi did not reduce GFP::LIN-3 expression in the AC and did not cause a Vul phenotype. (C,C') AC-specific expression of *sra-9::SL2::mCherry* from the single-copy MosSci transgene *zhIs143[P_{ACEL}>sra-9::SL2::mCherry]*. mCherry expression in a late L2 larva is shown. The scale bar in (C') is 10µm.

Supplementary methods

Plasmid constructs

pLM5 (*lin-3(zh112)* repair template)

The pDD268 plasmid (Dickinson et al., 2015) was digested with the AvrII and SpeI restriction enzymes, adding a linker to the 3' end of the fluorophore insertion site when recombined with the homology arms by means of the Gibson protocol (Gibson et al., 2009). The inserted homology arms were amplified by Phusion PCR from genomic *lin-3* DNA with the following oligonucleotide combinations: HA1: 0.7 kb with OLM181 (ACG TTG TAA AAC GAC GGC CAG TCG CCG GCA GAA GAG GTC ATA CAG CAA TGC ACA G) and OLM182 (CAT CGA TGC TCC TGA GGC TCC CGA TGC TCC GAG ACA CGA TTC TGA AAC TTT TAT TG) and 0.46 kb with HA2: OLM183 (CGT GAT TAC AAG GAT GAC GAT GAC AAG AGA CCT TCG TGG TTT CGT CAA GAA CGT AG) and OLM184 (GGA AAC AGC TAT GAC CAT GTT ATC GAT TTC CAG ACC TAA TCA AAT GGC TAC CTT TGC).

pLM12 (SGN3A for *lin-3(zh112)*)

Single guide SG3A sequence gtt ctt gac gaa acc acg aa was cloned through NEB's Q5 Site-Directed Mutagenesis Kit into pDD162 (Addgene plasmid # 47549) with OLM177 (gtt ctt gac gaa acc acg aaG TTT TAG AGC TAG AAA TAG CAA G).

pLM13 (SGN3B for *lin-3(zh112)*)

Single guide SG3A sequence cag aat cgt gtc tcc ctt cg was cloned through NEB's Q5 Site-Directed Mutagenesis Kit into pDD162 with OSS1 (cag aat cgt gtc tcc ctt cgG TTT TAG AGC TAG AAA TAG CAA G).

pLM6 (*nlp-26(zh113)* repair template)

The pDD282 plasmid (Addgene #66823) was digested with the AvrII and SpeI restriction enzymes, adding a linker to the 3' end of the fluorophore insertion site when recombined with the homology arms by means of the Gibson protocol (Gibson et al., 2009). The inserted homology arms were amplified by Phusion PCR from genomic *nlp-26* DNA with the following oligonucleotide combinations: HA1: 0.6 kb with OSS3 (acg ttg taa aac gac ggc cag tcg ccg gca TTG GCG GGA AAT TCA ATG TTT CAG TC) and OSS4 (CAT CGA TGC TCC TGA GGC TCC CGA TGC TCC tAG GGA GAA GAT CAC GAA GAA GTT C) and 0.6 kb with HA2: OSS5 (CGT GAT TAC AAG GAT GAC GAT GAC AAG AGA CTT CTT GTT GGC CTT GTA TCC GCA C) and OSS6 (gga aac agc tat gac cat gtt atc gat ttc CTG CTT GGT GTT ATA TTT GAA GGG TAT CAC).

pLM8 (SGN2 for *nlp-26(zh113)*)

Single guide N2 ATA CAA GGC CAA CAA GAA GG was cloned through NEB's Q5 Site-Directed Mutagenesis Kit 2 with primers OSS7 (CCT TCT TGT TGG CCT TGT ATG TTT TAG AGC TAG AAA TAG CAA G) into plasmid pDD162 (Addgene # 47549).

pLM9 (SGN3 for *nlp-26(zh113)*)

Single guide N3 ATA CAA GGC CAA CAA GAA GG was cloned through NEB's Q5 Site-Directed Mutagenesis Kit with primers OSS8 (TAC AAG GCC AAC AAG AAG GAG TTT TAG AGC TAG AAA TAG CAA G) into plasmid pDD162.

pLM10 (SGN4 for *nlp-26(zh113)*)

Single guide N4 sequence ATA CAA GGC CAA CAA GAA GG was cloned through NEB's Q5 Site-Directed Mutagenesis Kit with primers OSS9 (TCT TGT TGG CCT TGT ATC CGG TTT TAG AGC TAG AAA TAG CAA G) into plasmid pDD162.

pSS22 (*sra-9(zh151)* repair template)

The pDD282 plasmid was digested with the AvrII and SpeI restriction enzymes, adding a linker to the 5' end of the fluorophore insertion site when recombined with the homology arms by means of the Gibson protocol (Gibson et al., 2009). The inserted homology arms were amplified by Phusion PCR from genomic *sra-9* DNA with the following oligonucleotide combinations: HA1: 0.666 kb with OSS181 (ACG TTG TAA AAC GAC GGC CAG TCG CCG GCA CTG TTG GAG TAG GGG CAT TGA GAC ATT TG) and OSS182 (CAT CGA TGC TCC TGA GGC TCC CGA TGC TCC ACT CCA CAT aTT tTT CAT tTG aCT gAT ATG GTT CTC CTG AG) and 0.686 kb with HA2: OSS179 (CGT GAT TAC AAG GAT GAC GAT GAC AAG AGA TAA CAA GTT TAA AAA AAT TTC ATT GGA ACT TGA AG) and OSS180 (CAG CTA TGA CCA TTT ATC GAT TTC GCA TCC GAA CGC AAT GAA CTT TTT GAG CTC AC)

pSS20 (SGN1 *sra-9(zh151)*)

Single guide N1 sequence GAT GAA GAA CAT GTG GAG TT by cycle restriction-ligation with the primers OSS175 (ctt gTT AGC CAG ATG AAG AAC ATG) and OSS176 (aaa cCA TGT TCT TCA TCT GGC TAA) into plasmid pDD162.

pSS21 (SGN2 *sra-9(zh151)*)

Single guide N2 sequence GAT GAA GAA CAT GTG GAG TT was cloned by cycle restriction-ligation with the primers OSS177 (ctt gGA TGA AGA ACA TGT GGA GTT)

and OSS178 (aaa cAA CTC CAC ATG TTC TTC ATC) into plasmid pDD162.

pMMO10 (*zhIs67[gfp::lin-3]*)

The *gfp* coding sequences amplified with the primers OJE131 (AGT CGA CCT GCA GGC ATG CAA GCT gag aca cga ttc tga aac) and OJE132 (GGC ATG GAT GAA CTA TAC AAA cct tcg tgg ttt cgt caa) were inserted into the *lin-3* locus amplified with primers OMMO118 (ttt cct agg CAT CGT TGA CTG ACT CAT G) and OMMO119 (ttt cct agg CGA CAT CAA GGT TCA CGG) by fusion PCR and subcloned into the AvrII site of pCFJ151 (Frøkjær-Jensen et al., 2008). The extrachromosomal array *zhEx523* was generated by injecting 50 ng/μl of plasmid MMO10 together with 10 ng/μl pGH8, 2.5 ng/μl pCFJ90, 5 ng/μl pCFJ104 and 50 ng/μl pJL43.1 as co-injection markers, and *zhEx523* was integrated by gamma-irradiation to generate the *zhIs67[gfp::lin-3]* reporter.

pMW87 (*zhIs143[P_{ACEL Δpes10}>sra-9_{genomic}::SL2::mCherry::unc-54 3'UTR]*)

The anchor cell-specific enhancer element of *lin-3* (ACEL), which has been coupled to the minimal *Δpes-10* promoter, was amplified with GGT ACC AGA GCT CAC CTA GGC ACC TGT GTA TTT TAT GCT GG / GCA CAA GCT ATG GTA GCC ATA ATC AAT GCC TGA AAG TTA AAA ATT AC, and fused by Gibson assembly (Gibson et al., 2009) to the genomic region of *sra-9* (amplified with ATG GCT ACC ATA GCT TGT GCA TC / TTA ACT CCA CAT GTT CTT CAT CTG) and to *SL2::mCherry::unc-54 3'UTR* in pCFJ151 (amplified with GAA GAA CAT GTG GAG TTA AGC TGT CTC ATC CTA CTT TCA CCT AG / CCT AGG TGA GCT CTG GTA CCC TCT AG). Plasmid pMW87 was injected at a concentration of 50 ng/μl together with 10 ng/μl pGH8, 2.5 ng/μl pCFJ90, 5 ng/μl pCFJ104 and 50 ng/μl pJL43.1 as co-injection markers to generate a single-copy insertion on LGIII according to the MosSci protocol (Frøkjær-Jensen et al., 2008).

pMW89 (for *zhEx632*[*P_{nlp-26}::gfp::lacZ::unc-54 3'UTR*])

1.43 kb from the *nlp-26* regulatory region was amplified with CTT GGA AAT GAA ATA AGC TTC CGT GTT TGT ATG AAT TGG CTG TG / CTT TGG CCA ATC CCG GGG ATC AAT TCT AGA AAT TTT TAG TAC AAA AAT TTC and cloned into the BamHI and HindIII sites of pPD96.04 by Gibson assembly (Gibson et al., 2009). Plasmid pMW89 was injected at a concentration of 100 ng/μl together with 50 ng/μl pBluescript KS- as carrier DNA and 2.5 ng/μl pCFJ90 as co-injection marker to generate the extrachromosomal array *zhEx632*.

pMW98 (for *zhEx668.1* to *zhEx668.3*[*P_{cdh-3}::unc-40_{minigene}::gfp::unc-54 3'UTR*])

The minimal AC element *mk62-63* of the *cdh-3* regulatory region (Ziel et al., 2009) was amplified with CTT GGA AAT GAA ATC CTA GGT AGA GCA TGA TGT CCT TAC CTT G / CCG AAA TGT CGC AAA ATC ATA GCT CGG TAC CCT CCA AGC AAG and fused by Gibson assembly (Gibson et al., 2009) to the *unc-40_{minigene}::gfp::unc-54 3'UTR*, which had been amplified with GAT TTT GCG ACA TTT CGG TGA GTT C / GAC TCC AAG GAT GCG GAG TCT GTT CGG CTC AAT TAC AAA ATA C from genomic DNA and with ACT CCG CAT CCT TGG AGT CGT ACG / GTG CCA CCT GAC GTC TAA GAA ACC from *qyls66* (Ziel et al., 2009), and cloned into the vector backbone of pPD95.75 (amplified with CTT AGA CGT CAG GTG GCA CTT TTC / ACG CTA ACA ACT TGG AAA TGA AAT). The mutation R938L that was present in the coding frame of the *unc-40* cDNA of *qyls66* was corrected by site directed mutagenesis. Plasmid pMW98 was injected at a concentration of 50 ng/μl together with 150 ng/μl pBluescript KS+ as carrier DNA and 2.5 ng/μl pCFJ90 as co-injection marker to generate three independent extrachromosomal arrays *zhEx668.1* to *zhEx668.3*.